A Large-Eddy Simulation Study in WRF on Wind over Broadband Waves of Different Directions and Spreading Widths

TIANYI LI,[a] PEIYUN ZHU,[b] JEFFREY D. MIROCHA,[a] AND OLIVER B. FRINGER[b]

[a] *Atmospheric, Earth and Energy Division, Lawrence Livermore National Laboratory, Livermore, California*
[b] *Department of Civil and Environmental Engineering, Stanford University, Stanford, California*

(Manuscript received 23 July 2024, in final form 17 February 2025, accepted 4 March 2025)

ABSTRACT: We use the Weather Research and Forecasting (WRF) Model coupled with moving waves to conduct large-eddy simulations (LESs) of wind over broadband waves with different propagating directions and spreading widths. Our results show that wind-opposing waves can double the form drag, and the wave propagating direction affects the mean wind velocity, velocity variances, and pressure stress. On the other hand, waves with wider spread tend to reduce the form drag in the streamwise direction. Results further indicate that the wave direction can impact the bulk drag coefficient by as much as 25%, while the wave directional spreading width can change it by 5%. Based on our wave-phase-resolved simulations, we demonstrate that the parameterization of sea surface roughness is significantly influenced by the direction of wave propagation relative to the wind, a factor that the commonly used Charnock relation does not account for.

KEYWORDS: Wind waves; Air-sea interaction; Large eddy simulations

1. Introduction

The interaction between wind and ocean surface waves plays a critical role in shaping the dynamics of coastal environments. Airflow near the air–sea interface is constantly influenced by surface waves through wave-induced drag and terrain-induced flow modification (Belcher and Hunt 1998). The transfer of momentum and scalars at the air–sea interface, such as heat and gases, serves as a visible manifestation of the intricate coupling between Earth's atmosphere and ocean (Sullivan and McWilliams 2010). Comprehending wind–wave interaction is crucial to understanding and modeling the energy and mass transfer mechanisms at the air–sea interface as well as their broader implications for weather forecasting, climate modeling, coastal processes, and various engineering applications.

In large-scale modeling, previous studies have been focused on characterizing the mean wind profile, the sea surface roughness length, and the drag coefficient, based on wave properties such as the wave age (Charnock 1955; Johnson et al. 1998; Moon et al. 2004; Drennan et al. 2005), wave height, and wave steepness (Belcher et al. 1993; Taylor and Yelland 2001). Here, the wave age is defined as c/u_* or c/U_{10}, where c is the phase speed of the wave, u_* is the friction velocity of the wind, and U_{10} is the wind speed at 10 m above the sea surface. Wave steepness is defined as ka, where k is the wavenumber and a is the wave amplitude.

At scales smaller than $O(1)$ km, direct numerical simulations (DNSs) and large-eddy simulations (LESs) have been widely used to study the effect of waves on the wind. These studies can be generally categorized into two types: one-way coupled model, where surface waves are prescribed, and two-way coupled model, where wave dynamics and airflow are fully coupled. In one-way coupled model, prescribed waves serve as the lower boundary to study their effects on airflow. DNS and LES studies of wind over monochromatic waves have shown that surface waves significantly influence airflow characteristics, such as mean wind flow, vertical momentum fluxes, velocity variances, pressure distributions, wave-induced drag, and momentum transfer across the air–water interface. These effects are strongly dependent on wave age and steepness (e.g., Sullivan et al. 2000; Shen et al. 2003; Kihara et al. 2007; Yang and Shen 2010; Druzhinin et al. 2012; Hara and Sullivan 2015). Recently, wave-phase-resolved drag models have been developed within wall-modeled LES for real-world applications (Aiyer et al. 2023; Ayala et al. 2024). On the other hand, two-way coupled simulations allow airflow to influence wave dynamics, making them well suited for studying the impacts of wind on wave evolution. For example, DNS studies have demonstrated that wind can generate broadband surface waves when it blows over a calm water surface (Li and Shen 2022, 2023). Additionally, LES studies have investigated the long-term evolution of broadband surface waves interacting with air turbulence, providing insights into complex wind–wave interactions (Hao and Shen 2019).

In these studies, the wind and waves are aligned and traveling in the same direction. However, this rarely occurs in the real ocean due to the limited fetch and duration of the wind, and most of the time wind and waves are misaligned based on a 40-yr global reanalysis dataset (Hanley et al. 2010). Site-specific studies have also demonstrated the prevalence of wind–wave misalignment. Donelan et al. (1985) summarized from data measured in Lake Ontario and a large laboratory tank that the misalignment between waves at the spectral peak and the mean wind can be up to 50°, depending on the gradient in fetch. Fischer et al. (2011) analyzed data measured at the Dutch North Sea and observed that for wind speed lower than 10 m s^{-1}, wind–wave misalignment reached almost 120°, while for wind speeds higher than 20 m s^{-1}, the misalignment angle decreases to roughly 30°. Using 10 years of field measurements

---

Denotes content that is immediately available upon publication as open access.

Corresponding author: Tianyi Li, li100@llnl.gov

DOI: 10.1175/MWR-D-24-0131.1

in the German Bight of the North Sea, Hildebrandt et al. (2019) concluded that wind and waves are aligned with ±15° deviation just 25% of the time, the strongest misalignment of 90° (±15°) occurs 10% of the time, and 65% of the time the misalignment angle is in between. Another scenario of wind–wave disequilibrium occurs when the wave is aligned with but travels in the opposite direction as the wind. Wind-opposing waves can occur under storm conditions, where wind direction changes rapidly, or under moderate weather conditions (Bowers et al. 2000; Wright et al. 2001; Ardhuin et al. 2007). These findings highlight the importance of understanding the effect of wind–wave disequilibrium on the wind to better characterize the atmospheric boundary layer in realistic scenarios.

Understanding wind–wave misalignment has a wide range of engineering applications, including the design, construction, and maintenance of offshore infrastructure, work vessel operations, and offshore wind power extraction (Hildebrandt et al. 2019). For wind energy specifically, although wind–wave misalignment has negligible effects on the power generation of floating offshore wind turbines, it significantly affects the motion and the structural load of wind turbines (Li et al. 2020). Wind and wave loads acting simultaneously from different directions also intensify fatigue damage on fixed offshore wind converters (Koukoura et al. 2016). Active research is being conducted on performance evaluation and design optimization of offshore wind turbines under conditions of misaligned wind and waves (e.g., Fischer et al. 2011; Kalvig et al. 2014; Wei et al. 2017). Therefore, a thorough understanding of the interactions between nonequilibrated wind and waves will greatly benefit the development of offshore wind energy.

Nonequilibrated wind and waves have gained attention in more recent studies. Cao et al. (2020) and Husain et al. (2022a) employed LES over monochromatic wind-opposing waves and showed enhanced pressure drag compared to wind-following waves. The change in airflow dynamics due to varying wave age is smoother for wind-opposing waves than wind-following waves (Husain et al. 2022a). Husain et al. (2022b) investigated the influence of very young (small wave age), steep ($ka = 0.27$), monochromatic waves misaligned with the wind at different angles and found that the pressure drag decreases as the angle between the wind and the wave increases, roughly following a $\cos^2\theta$ trend based on theoretical studies (e.g., Burgers and Makin 1993; Li et al. 2000). Misaligned waves also lead to enhanced wind shear throughout the wave boundary layer and enhanced wind speed farther from the surface (Husain et al. 2022b). Deskos et al. (2022) conducted DNS over wind-following, wind-opposing, and misaligned monochromatic waves and found marginal differences in wave-induced velocity for misaligned waves compared to aligned waves but large differences for wind-opposed waves, consistent with Cao et al. (2020). To our knowledge, the only study on misaligned broadband waves is that of Patton et al. (2019), using LES and a wave field of combined seas and swell. Their analysis focuses on swells and showed that misaligned swells change the angle between wind and stress vectors and increase the surface pressure drag, with an angle of 180° (wind-opposing waves) having the largest effect. These effects are smaller as the wave age decreases.

In this study, we investigate the influence of misaligned broadband waves with different angles and degrees of spreading on the atmospheric boundary layer. Wave directional spreading is the angular distribution of waves relative to the main wave-propagating direction. The wave spreading width quantifies the deviation of wave directions from a single propagation direction. This parameter is essential for assessing real-world oceanic conditions where waves often propagate in a spectrum of directions. Idealized studies commonly assume unidirectional wave fields, providing important foundational insights on wind–wave interactions (e.g., Hara and Sullivan 2015; Cao et al. 2020). However, realistic wave fields involve a spectrum of directions, making the wave spreading angle crucial for understanding natural ocean dynamics. Despite the prevalence of misaligned seas in nature (e.g., Hasselmann et al. 1973; Donelan et al. 1985; Hanley et al. 2010), the effect of the propagating direction of the spectral peak wave relative to the wind and the degree of directional spreading has not been explored. We use LES in the Weather Research and Forecasting (WRF) Model to couple the wind to a prescribed wave field. WRF is a mesoscale numerical weather prediction model that has been extensively utilized in atmospheric research and operational applications (Skamarock et al. 2019). An LES capacity is also provided in WRF with a number of subgrid-scale turbulence options. In Zhu et al. (2023), the ability of WRF–LES to simulate wind over moving waves is described along with a validation of the moving wave implementation with monochromatic waves. In this paper, the moving wave capacity is further extended to broadband waves. Because the effects of misaligned waves on mean wind and wind stress are much smaller for angles smaller than 90° (Patton et al. 2019), we initialize broadband wave fields with dominant propagating directions of 0°, 90°, and 180° relative to the positive streamwise direction and each with spreading widths of 20°, 40°, and 90°.

This paper is organized as follows. Section 2 describes the numerical method of WRF coupled with moving wave and the simulation setup. Section 3 discusses the characteristics of the wind over the broadband wave fields of different degrees of misalignment and directional spreading, including the mean wind, wind stresses, turbulent statistics, and wave growth rate. Finally, section 4 summarizes the major findings and discusses potential future work.

2. Method

a. WRF–LES over moving waves

WRF solves the compressible Navier–Stokes equations and transport equations for temperature, moisture, and tracers. WRF supports simulations of flow over complex terrain with moderate slopes and flow over multiple scales from turbulence resolving to synoptic, using a pressure-based curvilinear coordinate. We use WRF v3.8.1, where the pressure-based curvilinear coordinate system is defined by

$$\tau = t,\ \xi = x,\ \eta = y,\ \zeta = \frac{p_h - p_{h,\mathrm{top}}}{\mu}, \tag{1}$$

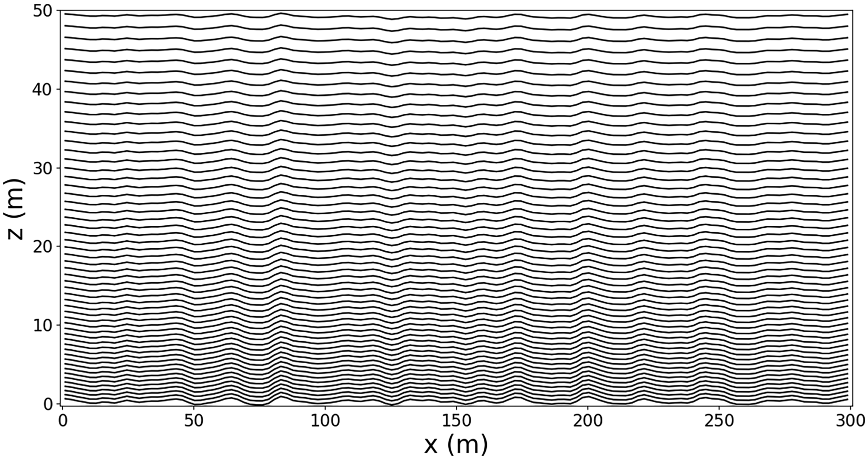

FIG. 1. A schematic of the vertical coordinate in WRF over broadband waves, showing the lowest 50 m in a domain with a height of 100 m.

where τ is the time in the transformed coordinate system; (ξ, η, ζ) are the spatial coordinates; the subscript h denotes hydrostatic variables; $\mu = p_{h,s} - p_{h,\mathrm{top}}$ is the difference between the hydrostatic pressure at the surface $p_{h,s}$ and the hydrostatic pressure at the top of the domain $p_{h,\mathrm{top}}$; and μ represents the dry air mass per unit area. Figure 1 shows a schematic of the vertical coordinate in WRF over broadband waves.

The governing equations in WRF are written in conservative flux form, with conservative fluxes defined as

$$\mathbf{U} = \mu\mathbf{u} = (U, V, W), \tag{2}$$

where $\mathbf{u}$ is the Cartesian velocity vector. The cross-coordinate flux is defined as

$$\Omega = \mu\frac{d\zeta}{dt}. \tag{3}$$

At the bottom $[z = h(x, y, t)$, where h is the water surface elevation], the cross-coordinate flux satisfies $\Omega = 0$. The momentum equations in the pressure-based curvilinear coordinate system are given by

$$\frac{\partial U}{\partial \tau} + \frac{\partial}{\partial \xi}(Uu) + \frac{\partial}{\partial \eta}(Vu) + \frac{\partial}{\partial \zeta}(\Omega u) + \mu\alpha\frac{\partial p}{\partial \xi} + \frac{\partial p}{\partial \zeta}\frac{\partial \phi}{\partial \xi} = F_U, \tag{4a}$$

$$\frac{\partial V}{\partial \tau} + \frac{\partial}{\partial \xi}(Uv) + \frac{\partial}{\partial \eta}(Vv) + \frac{\partial}{\partial \zeta}(\Omega v) + \mu\alpha\frac{\partial p}{\partial \eta} + \frac{\partial p}{\partial \zeta}\frac{\partial \phi}{\partial \eta} = F_V, \tag{4b}$$

$$\frac{\partial W}{\partial \tau} + \frac{\partial}{\partial \xi}(Uw) + \frac{\partial}{\partial \eta}(Vw) + \frac{\partial}{\partial \zeta}(\Omega w) - g\left(\frac{\partial p}{\partial \zeta} - \mu\right) = F_W, \tag{4c}$$

where $\phi = gz$ is the nonconservative geopotential; $\alpha = 1/\rho$ is the inverse density; and F_U, F_V, and F_W are the forcing terms that include turbulent mixing, Coriolis force, buoyancy, and model physics (e.g., microphysics of clouds, radiation, and planetary boundary layer models). In this paper, the forcing terms are given by

$$F_U = \frac{\partial}{\partial \xi_k}\left(\mu\tau_{1j,\mathrm{SGS}}\frac{\partial \xi_k}{\partial x_j}\right) + \frac{1}{\rho_0}\frac{dP}{dx}, \tag{5a}$$

$$F_V = \frac{\partial}{\partial \xi_k}\left(\mu\tau_{2j,\mathrm{SGS}}\frac{\partial \xi_k}{\partial x_j}\right), \tag{5b}$$

$$F_W = \frac{\partial}{\partial \xi_k}\left(\mu\tau_{3j,\mathrm{SGS}}\frac{\partial \xi_k}{\partial x_j}\right), \tag{5c}$$

where $(\xi_1, \xi_2, \xi_3) = (\xi, \eta, \zeta)$; $\tau_{ij,\mathrm{SGS}}$ is the subgrid scale (SGS) stress; and $\rho_0^{-1}dP/dx$ is the constant pressure gradient forcing.

The governing equation for mass conservation is given by

$$\frac{\partial \mu}{\partial \tau} + \frac{\partial U}{\partial \xi} + \frac{\partial V}{\partial \eta} + \frac{\partial \Omega}{\partial \zeta} = 0, \tag{6}$$

and the kinematic condition or the geometric conservation law (GCL) is given by

$$\frac{\partial \phi}{\partial \tau} + \frac{1}{\mu}\left(U\frac{\partial \phi}{\partial \xi} + V\frac{\partial \phi}{\partial \eta} + \Omega\frac{\partial \phi}{\partial \zeta} - gW\right) = 0. \tag{7}$$

The lower boundary $(z = h)$ satisfies the no-normal flow condition and can be derived from Eq. (7) as

$$W = \mu\frac{\partial h}{\partial t} + U\frac{\partial h}{\partial \xi} + V\frac{\partial h}{\partial \eta}. \tag{8}$$

As for boundary conditions over a rough wall, we adapt the quadratic drag law to a moving bottom by computing the stress based on the relative velocity between the air and the water, which is given by

$$\mathbf{u}_r = \mathbf{u} - \mathbf{u}_w, \tag{9}$$

where $\mathbf{u}_w$ is the velocity of the water at $z = h$. The horizontal components of the stress by the water on the flow are given by (e.g., Yang et al. 2013; Sullivan et al. 2014; Hao and Shen 2019)

$$\tau_{13} = C_d|\mathbf{u}_r|u_{\parallel}, \tag{10a}$$

$$\tau_{23} = C_d|\mathbf{u}_r|v_{\parallel}, \tag{10b}$$

where the components of velocity parallel to the water surface are given by

$$u_{\parallel} = \frac{u_r + w_r(\partial h/\partial \xi)}{\sqrt{(\partial h/\partial \xi)^2 + 1}}, \tag{11a}$$

$$v_{\parallel} = \frac{v_r + w_r(\partial h/\partial \eta)}{\sqrt{(\partial h/\partial \eta)^2 + 1}}, \tag{11b}$$

and the drag coefficient C_d is determined such that the horizontal velocity in the bottom-most grid cell (at $z = h + \Delta z/2$) satisfies the log law:

$$C_d = \left[\frac{\kappa}{\ln \Delta z/(2z_0)}\right]^2, \tag{12}$$

where $\kappa = 0.4$ is the von Kármán constant and z_0 is the background roughness length. We use a typical background roughness value for the open ocean, $z_0 = 0.0002$ m, in wave-phase-resolved wall-modeled LES (Sullivan et al. 2008; Jiang et al. 2016; Hao and Shen 2019). The details of the implementation of the coupled WRF–LES and moving waves can be found in Zhu et al. (2023). Our model directly solves the compressible LES equations with an explicit moving wave boundary in a wave-surface-fitted grid to resolve wind–wave interactions. A sensitivity analysis of different background surface roughnesses on the mean wind statistics and wave growth rate is provided in section b of the appendix.

b. Synthetic wave field

We initialize the broadband wave field using the Joint North Sea Wave Project (JONSWAP) spectrum (Hasselmann et al. 1973). It is empirically derived from a field campaign that obtained months of ocean surface wave and wind data (Hasselmann et al. 1973) and captures the spectrum of early stage seas under limited fetch. The JONSWAP spectrum is expressed as

$$E_J(k) = \frac{\alpha_J g^2}{\omega^5}\exp\left[-\frac{5}{4}\left(\frac{\omega_p}{\omega}\right)^4\right]\gamma^r, \tag{13}$$

where ω_p is the wave frequency at the spectral peak, i.e., the peak wave frequency, and is determined from the wind input with

$$\omega_p = 22\left(\frac{g^2}{U_{10}F}\right)^{1/3}, \tag{14}$$

with U_{10} being the wind speed at a height of 10 m above the sea surface and F being the fetch. The peak wave frequency is related to the peak wavenumber k_p through the dispersion relation for deep-water waves:

$$\omega_p = \sqrt{gk_p}. \tag{15}$$

The other parameters in Eq. (13) are defined as

$$r = \exp\left[-\frac{(\omega - \omega_p)^2}{2\sigma^2\omega_p^2}\right], \tag{16a}$$

$$\alpha_J = 0.076\left(\frac{U_{10}^2}{gF}\right)^{0.22}, \tag{16b}$$

where $\gamma = 3.3$ and

$$\sigma = \begin{cases} 0.07, & \omega \le \omega_p, \\ 0.09, & \omega > \omega_p. \end{cases} \tag{17}$$

The directional spectrum is generally assumed to be the JONSWAP spectrum multiplied by a spreading function $D(\theta)$ (Longuet-Higgins 1963). We use a directional spreading function of the form:

$$D(\theta) = \begin{cases} \dfrac{2}{\Theta}\cos^2\left[\dfrac{\pi(\theta - \theta_0)}{\Theta}\right], & |\theta - \theta_0| \le \dfrac{\Theta}{2}, \\ 0, & |\theta - \theta_0| > \dfrac{\Theta}{2}, \end{cases} \tag{18}$$

where θ_0 is the primary propagation direction and Θ is the directional spreading width. For example, $\theta_0 = 0°$ and $\Theta = 20°$ imply that the wave spectrum lies from $-10°$ to $10°$ in frequency–angle ω–θ space and is centered around 0°. In the present study, we choose broadband wave fields with primary propagation directions of 0°, 90°, and 180° relative to the positive streamwise direction (the positive x direction) and each with spreading widths of 20°, 40°, and 90°. Figure 2 displays spectra in ω–θ space for the cases in which the primary propagation direction is 0° and 90°. The corresponding wave fields are shown in Fig. 3.

Similar to Sullivan et al. (2014) and Patton et al. (2019), we advance the waves synthetically in time by assuming a linear superposition of different wave components with

$$h(\mathbf{x}, t) = \sum_{\mathbf{k}} a(k)\cos[\mathbf{k}\cdot\mathbf{x} - \omega(k)t + \varphi(\mathbf{k})], \tag{19}$$

where $k = |\mathbf{k}|$ is the amplitude of the wavenumber vector and $\varphi(\mathbf{k})$ is a random phase. The amplitude of each wave component is given by

$$a(k) = \sqrt{E_J(k)D(\theta)dk_x dk_y}. \tag{20}$$

The assumption of linearly superimposed waves is consistent with the nature of one-way coupling of the wind and the waves, by which the wind is affected by the waves, whereas

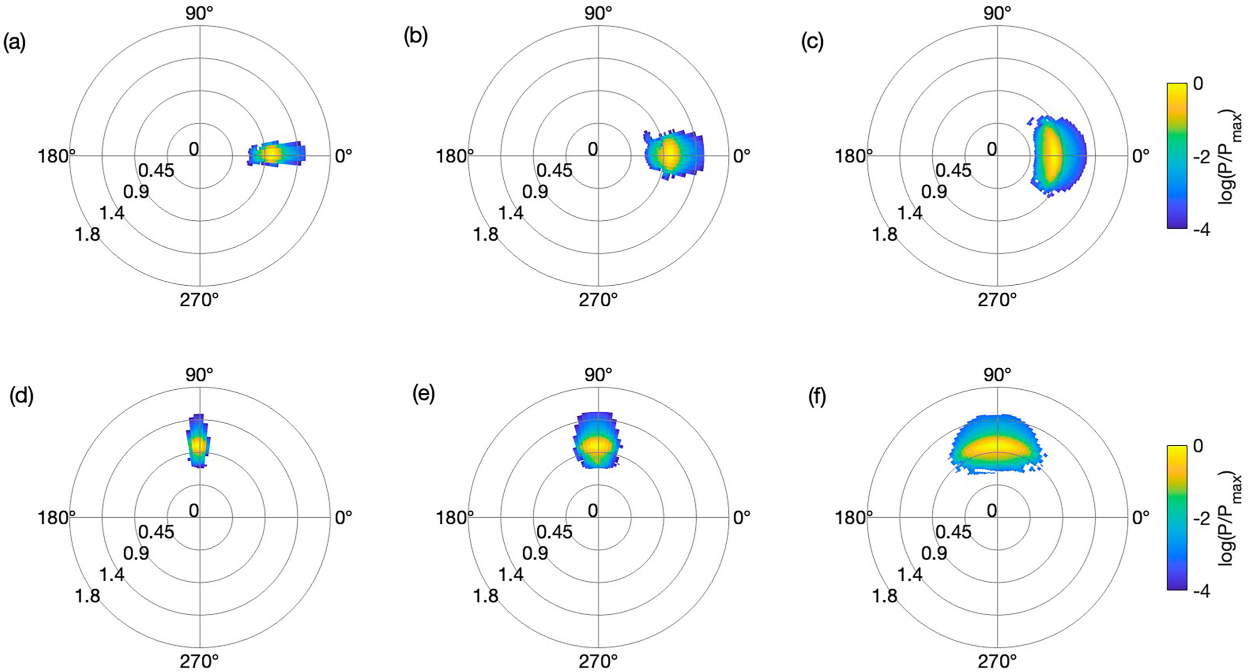

FIG. 2. Wave spectra in ω–θ space with (a) $\theta_0 = 0°$, $\Theta = 20°$; (b) $\theta_0 = 0°$, $\Theta = 40°$; (c) $\theta_0 = 0°$, $\Theta = 90°$; (d) $\theta_0 = 90°$, $\Theta = 20°$; (e) $\theta_0 = 90°$, $\Theta = 40°$; and (f) $\theta_0 = 90°$, $\Theta = 90°$, normalized by their maximum values. The contours display the logarithm of the normalized spectra. The radial direction is the wave frequency normalized by the peak frequency ω/ω_p.

the waves are not affected by the wind. Previous studies have shown that the two-way coupling of wind and waves plays a minor role in the influence of waves on wind turbulence. Yang and Shen (2009) compared one- and two-way coupled wind and waves using DNS to resolve the wind and a high-order spectral (HOS) method to resolve the waves. They found that the difference in the airflow vortical structures between the two types of coupled models is negligible. Cao et al. (2023) also

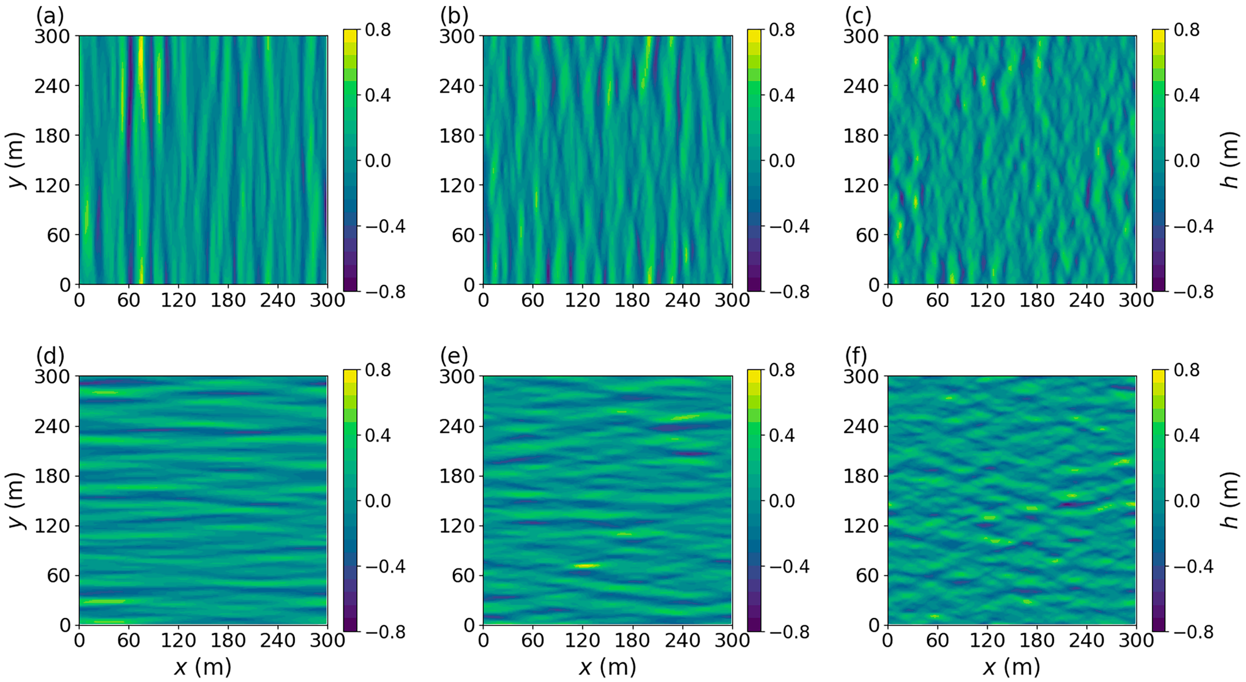

FIG. 3. Surface plots of the wave height initialized with the JONSWAP directional spectrum with (a) $\theta_0 = 0°$, $\Theta = 20°$; (b) $\theta_0 = 0°$, $\Theta = 40°$; (c) $\theta_0 = 0°$, $\Theta = 90°$; (d) $\theta_0 = 90°$, $\Theta = 20°$; (e) $\theta_0 = 90°$, $\Theta = 40°$; and (f) $\theta_0 = 90°$, $\Theta = 90°$.

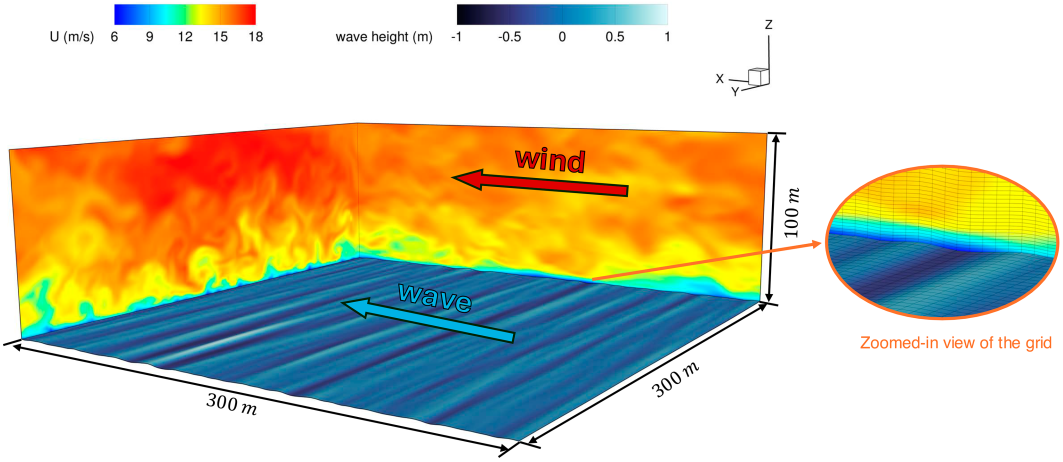

FIG. 4. Instantaneous snapshot of wind over broadband ocean surface waves. Contours plotted in the vertical planes represent the streamwise velocity of the airflow, and contours in the horizontal plane show the surface wave height. Both the wind and the waves propagate in the x direction. The zoomed-in view on the right illustrates the surface-fitted grid above the ocean surface waves.

showed that the fundamental mode of the airflow perturbation arises mainly from the linear components of the wave. On the other hand, Hao and Shen (2019) examined long-term wave evolution using two-way coupled LES simulations over broadband JONSWAP wave fields. They observed that the downshift of the peak spectral frequency over roughly 3000 peak wave periods is less than 10%, and the shape of the wave spectrum remains largely unchanged. As illustrated in Zhu et al. (2023), one-way coupled models are also computationally more efficient than two-way coupled models. These findings suggest that it is reasonable to use a one-way coupled model to study the effect of waves on the wind. In this study, we do not account for flow separation in our analysis because the wave steepness is relatively small. The grid resolution and wave properties in the present study indicate that such effects are negligible in our simulations. As highlighted in previous studies (e.g., Buckley and Veron 2016), flow separation tends to occur with larger wave steepness, generating a region of reduced air velocity on the downwind side of the wave crest.

c. Model setup

The WRF–LES simulations in this study have a computational domain of 300 m × 300 m × 100 m, with 128 × 128 × 80

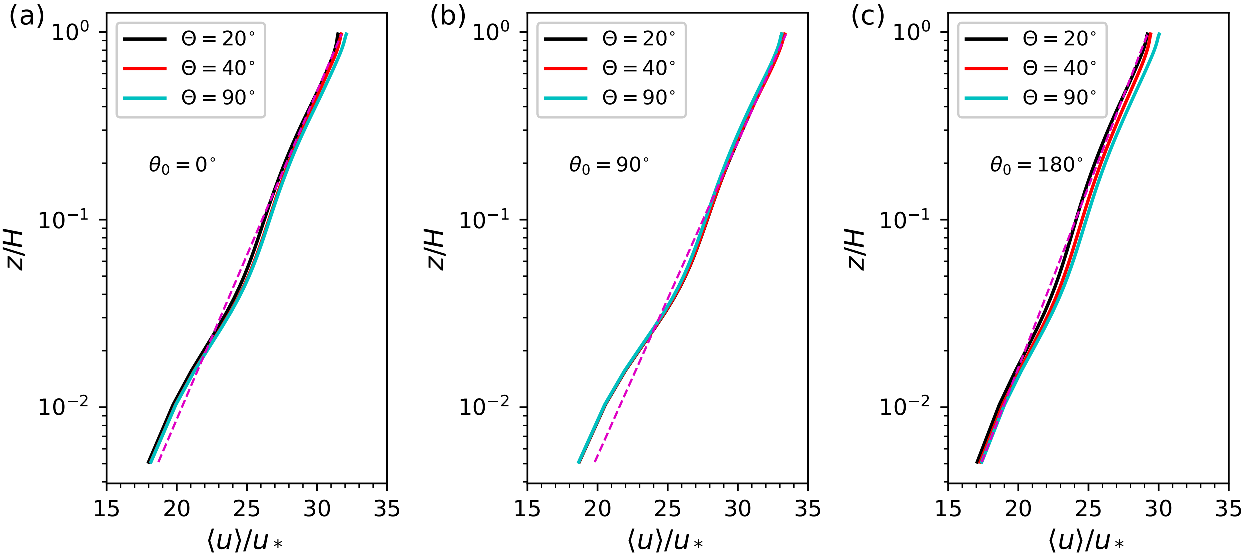

FIG. 5. Mean streamwise velocity normalized by u_* for wave propagation directions: (a) $\theta_0 = 0°$, (b) $\theta_0 = 90°$, and (c) $\theta_0 = 180°$. The colors black, red, and cyan represent wave spreading widths of $\Theta = 20°$, 40°, and 90°, respectively. The magenta line with circles is the fitted log profile.

grid points in the streamwise (x), spanwise (y), and vertical (z) directions. The horizontal grid spacing is $\Delta x = \Delta y = 2.3$ m, resulting in about 11 points per peak wavelength. The horizontal grid resolution related to peak wavelength is consistent with previous studies of wall-modeled LES of wind over waves (e.g., Hao and Shen 2019; Aiyer et al. 2023; Ayala et al. 2024). The vertical grid spacing is $\Delta z = 0.5$ m at the bottom and then gradually stretched as the height increases. This vertical grid spacing near the wave surface is finer than the 1-m spacing used by Sullivan et al. (2008) and the 7.8-m spacing used by Yang et al. (2014). Additionally, it is comparable to the 0.39-m vertical spacing reported by Hao and Shen (2019). We further conduct a sensitive analysis on the grid resolution by running an additional case with a 256 × 256 × 160 grid. The details of this analysis are provided in the appendix. For the JONSWAP spectrum, we set $U_{10} = 4$ m s^{-1} and $F = 66$ km, resulting in a broadband wave field with $k_p = 0.25$ m^{-1}. The flow is forced by a constant horizontal pressure gradient with the same value for all cases, leading to a friction velocity $u_* = \sqrt{H\rho_0^{-1}dP/dx} = 0.53\,\mathrm{m\,s^{-1}}$, where H is the domain height. The turbulent eddy viscosity is computed with the Smagorinsky turbulence closure scheme. The time step of the model is 0.009 s based on the CFL constraint in terms of the sound speed, as WRF resolves sound waves explicitly [see details in Zhu et al. (2023)]. We ran the simulations for three wave-propagating directions, $\theta_0 = 0°$, $90°$, and $180°$, and three wave spreading widths, $\Theta = 20°$, $40°$, and $90°$, for each of the directions. To study the effect of wind–wave misalignment, an angle of $\theta_0 = 90°$ is chosen because the effect of waves propagating at an angle of 45° is much smaller than that of waves propagating at an angle of 90°. The wave spreading widths are sampled to represent waves with narrow spreading ($\Theta = 20°$), intermediate spreading ($\Theta = 40°$), and wide spreading ($\Theta = 90°$). All runs reached turbulence equilibrium after 70–80 eddy turnover periods ($H/u_* = 188\,\mathrm{s} = 47T_p$, where $T_p = 2\pi/\omega_p$), and we compute turbulence statistics using data from 30 eddy turnover periods after equilibrium is reached. As for gravity waves, wavenumber components with different wavenumber magnitudes propagate at different speeds. We have run each case over 4300 peak wave periods, and our sampling duration spans over 1300 wave periods of the peak waves. Given this extended simulation and sampling duration, the influence of initial phases of different wave components in the initialization of the wave field becomes negligible. We have conducted an additional run with a different wavefield initialization while keeping all physical parameters the same. The results show negligible differences in turbulence statistics between the two runs. Figure 4 shows an instantaneous flow field from our simulation of wind over broadband waves.

The Coriolis force is not included to reduce the computational cost of the simulations. The Ekman layer thickness (based on u_*/f_c, where f_c is the Coriolis parameter) is $O(1000)$ m or greater, which would require a much larger computational domain. Furthermore, the time scale for transient inertial oscillations to decay, which would be many inertial periods $f_c^{-1} = O(10^4)$ s, would significantly increase the computation time needed to reach equilibrium. Although Coriolis effects would produce the Ekman spiral and wind stress that is misaligned with the pressure gradient forcing, those effects do not change the overall findings of this investigation.

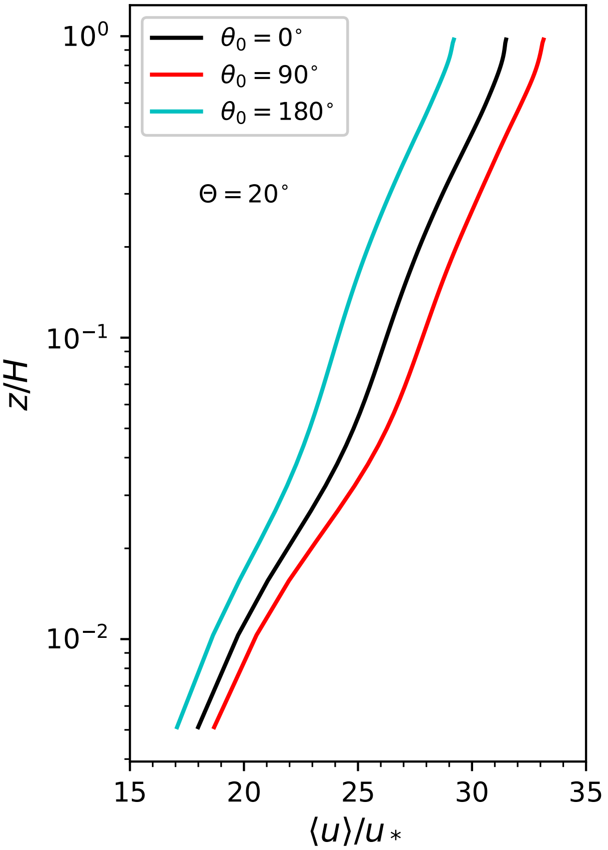

FIG. 6. Mean streamwise velocity normalized by u_* for wave propagation directions of $\theta_0 = 0°$ (black), $\theta_0 = 90°$ (red), and $\theta_0 = 180°$ (cyan). All three cases have the wave spreading width of $\Theta = 20°$.

3. Results

To compute the turbulence perturbation, we decompose a physical quantity f with

$$f = \langle f\rangle(\zeta) + f'(\xi, \eta, \zeta, t), \tag{21}$$

where $\langle f\rangle$ is the average in time and the horizontal and f' is the turbulent fluctuation. Note that the wave-induced perturbation cannot be separated from the turbulent perturbation with the triple decomposition employed in studies with monochromatic waves (e.g., Yang and Shen 2009; Cao and Shen 2021; Zhu et al. 2023). The triple decomposition requires the reference frame to be shifted to a wave-following frame, which cannot be achieved when the waves are broadband. Therefore, the turbulent perturbation presented here includes wave-induced effects.

Figure 5 shows the mean streamwise velocity profiles for all nine cases. The spreading width Θ has a small effect on the mean wind magnitude, although it increases slightly with Θ for $\theta_0 = 0°$ and 180°. This trend can be explained by the comparison of total drag and the pressure drag among all cases which

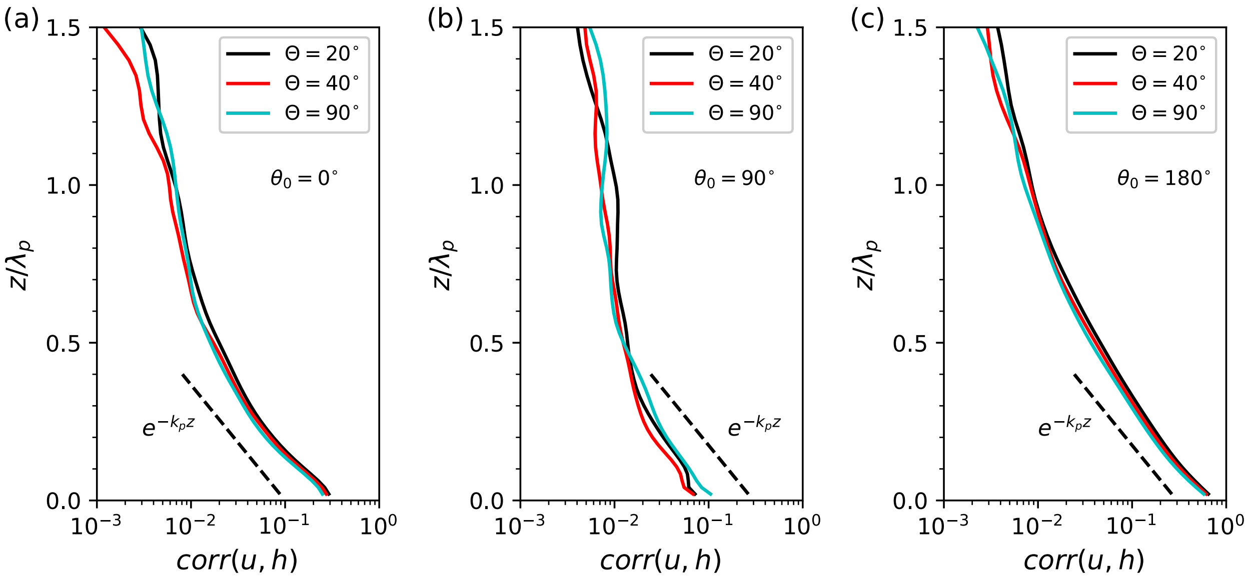

FIG. 7. Correlation between the streamwise velocity u and the wave height h for wave propagation directions: (a) $\theta_0 = 0^\circ$, (b) 90°, and (c) 180°. The colors black, red, and cyan represent wave spreading widths of $\Theta = 20^\circ$, 40°, and 90°, respectively. The black dashed lines indicate the trend of $e^{-k_p z}$, where k_p represents the peak wavenumber.

is discussed later. As for the effect of the wave-propagating direction, Fig. 6 compares the mean streamwise velocity across different propagating directions θ_0, with fixed $\Theta = 20^\circ$. As expected, the wind-opposing waves ($\theta_0 = 180^\circ$) lead to the lowest mean wind due to the highest drag from the waves on the wind. Waves propagating in the y direction ($\theta_0 = 90^\circ$) do not apply strong drag to the wind in the x direction, along which the wind is forced by a constant pressure gradient, and therefore lead to the highest mean wind. The comparison across wave-propagating directions is similar for cases with $\Theta = 40^\circ$ and 90° (not shown).

The correlation between the streamwise velocity u and the wave height h is presented in Fig. 7 to show the effect of waves on the wind. The correlation is defined as

$$\mathrm{corr}(u, h) = \frac{\langle u'h \rangle}{\sqrt{\langle u'^2 \rangle \langle h^2 \rangle}}, \qquad (22)$$

where u' is computed using Eq. (21). Figures 7a–c show that for all combinations of propagating direction and wave spreading width, the correlation between u and h decays exponentially with height over a length scale dictated by the peak wavelength. This behavior aligns with the trend of $e^{-k_p z}$, as previously reported by Hao and Shen (2019). The wave spreading width has little effect on corr(u, h), while the propagating direction has a significant effect. At the bottom, u and h are strongly correlated for $\theta_0 = 0^\circ$ and $\theta_0 = 180^\circ$, with 30% and 60% correlation, respectively. This indicates that the wind is heavily influenced by the waves for waves aligned with the wind, and the effect of waves is mostly confined below a height of one peak wavelength $\lambda_p = 2\pi/k_p$. For $\theta_0 = 90^\circ$, the correlation between u and h is very low as expected. However, the correlation between the spanwise velocity v and the wave height h for this case is strong, as shown in Fig. 8.

We next investigate the effects of the propagation direction θ_0 and the wave spreading width Θ on velocity variances. Figure 9 compares velocity variances for different θ_0 values with Θ fixed at 20°. The velocity variances $\langle u'^2 \rangle$ and $\langle v'^2 \rangle$ are negligibly affected by the propagating angle θ_0. However, $\langle w'^2 \rangle$ has similar values for both $\theta_0 = 0^\circ$ and 180° but decreases by up to two-thirds for $\theta_0 = 90^\circ$ compared to the wind-following and wind-opposing cases. This is expected because waves perpendicular to the wind interact less with the wind and cause less perturbation in wind velocity. Figure 10 further illustrates $\langle w'^2 \rangle$ for varying θ_0 and Θ. For $\theta_0 = 0^\circ$ and $\theta_0 = 180^\circ$ (Figs. 10a,c), $\langle w'^2 \rangle$ decreases as Θ increases, which supports the above analysis. When the waves are perpendicular to the wind ($\theta_0 = 90^\circ$), the larger the waves spread, the more aligned they will be with the wind, thus resulting in larger vertical velocity variance, as shown in Fig. 10b.

With the definition of the turbulence perturbation, averaging the streamwise momentum in Eq. (4a) gives the momentum budget in the streamwise direction:

$$\langle \tau_{13}^T \rangle + \langle \tau_{13}^p \rangle + \langle \tau_{13}^{\mathrm{SGS}} \rangle = \tau_{\mathrm{tot}}. \qquad (23)$$

Defining $U_3 = w - u(\partial z/\partial \xi) - v(\partial z/\partial \eta)$ as the contravariant velocity normal to the ζ surfaces, the Reynolds stress is defined as

$$\langle \tau_{13}^T \rangle = -\langle u' U_3' \rangle, \qquad (24)$$

the pressure stress (the form drag is $\langle \tau_{13}^p \rangle$ evaluated at $z = 0$) is defined as

$$\langle \tau_{13}^p \rangle = \left\langle \frac{p}{\rho} \frac{\partial z}{\partial \xi} \right\rangle, \qquad (25)$$

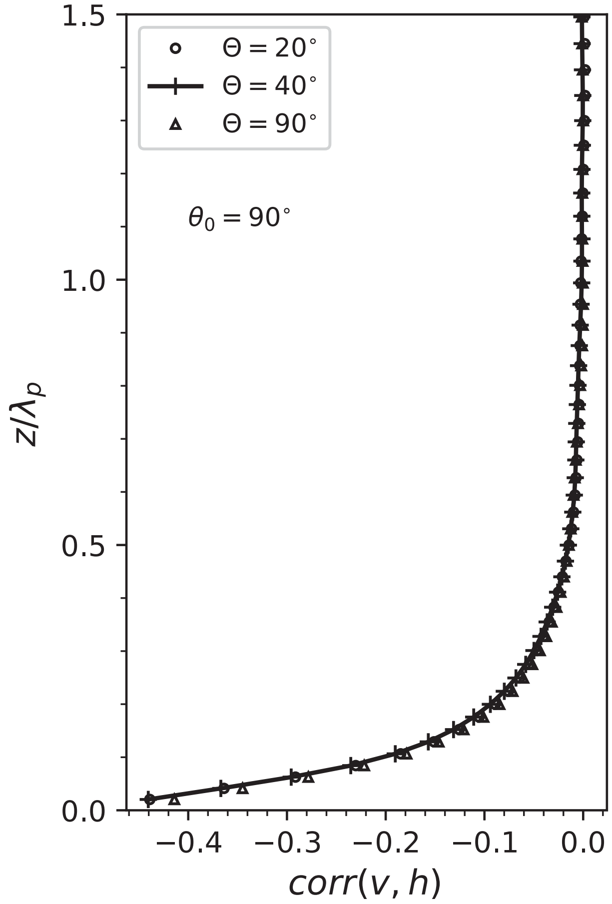

FIG. 8. Correlation between the spanwise velocity v and the wave height h, for wave propagation direction of $\theta_0 = 90^\circ$ and wave spreading widths of $\Theta = 20^\circ$ (circles), 40° (pluses), and 90° (triangles).

the SGS stress is defined as

$$\langle \tau_{13}^{\mathrm{SGS}} \rangle = -\left\langle \tau_{13,\mathrm{SGS}} - \tau_{11,\mathrm{SGS}}\frac{\partial z}{\partial x} - \tau_{12,\mathrm{SGS}}\frac{\partial z}{\partial y} \right\rangle, \tag{26}$$

and the total stress in the streamwise direction is

$$\tau_{\mathrm{tot}} = u_*^2\left(1 - \frac{z}{H}\right). \tag{27a}$$

A detailed derivation of Eq. (23) can be found in Hara and Sullivan (2015) and Zhu et al. (2023).

Figure 11 shows the profiles of Reynolds stress $\langle \tau_{13}^T \rangle$, SGS stress $\langle \tau_{13}^{\mathrm{SGS}} \rangle$, and pressure stress $\langle \tau_{13}^p \rangle$ for different wave-propagation directions θ_0. The Reynolds stress and SGS stress exhibit only slight differences for different propagating directions (Figs. 11a,b) and are unaffected by the spreading width (plots not shown). However, the spreading width has a more prominent effect on the pressure stress $\langle \tau_{13}^p \rangle$. The pressure stress is roughly doubled in the wind-opposing case ($\theta_0 = 180^\circ$) compared to the wind-following case ($\theta_0 = 0^\circ$) and near zero in the case with $\theta_0 = 90^\circ$. The pressure stress is balanced by the SGS stress at the bottom. Consequently, the case with $\theta_0 = 90^\circ$ has the largest SGS stress at the bottom and the wind-opposing case has the lowest. In contrast, the wave-propagating direction θ_0 has a negligible influence on the Reynolds stress $\langle \tau_{13}^T \rangle$. Figure 12 further shows the profiles of pressure stress $\langle \tau_{13}^p \rangle$ for different wave propagation direction θ_0 and wave spreading width Θ combinations. For $\theta_0 = 0^\circ$ and 180° (Figs. 12a,c), the pressure stress at the bottom, or the form drag, decreases with increasing Θ, and the form drag for $\Theta = 90^\circ$ is roughly 15% smaller than for $\Theta = 20^\circ$. The reduction in the form drag can be explained by the fact that as the waves spread, the spanwise component of the wave slope ($|\partial h/\partial y|$) increases, while the streamwise component ($|\partial h/\partial x|$) decreases. In the case where $\theta_0 = 90^\circ$, the wave height varies mostly in the spanwise rather than the streamwise direction, resulting in the form drag that is one order of magnitude lower than the cases in which the wave-propagating direction is aligned with the streamwise direction (Fig. 12b). Contrary to the cases where $\theta_0 = 0^\circ$ or 180°, as wave spreading width Θ increases, the waves spread more toward the streamwise direction and $|\partial h/\partial x|$ increases, causing enhanced form drag. Although there is a spanwise pressure stress driven by the waves perpendicular to the wind, without a spanwise pressure gradient forcing, the mean spanwise velocity and stress components in the spanwise momentum budget are negligible compared to those in the streamwise direction. The contribution of form drag $\langle \tau_{13}^p \rangle|_{z=0}$ to the total drag in our simulations, denoted as normalized form drag $\langle \tau_{13}^p \rangle|_{z=0}/u_*^2$, is approximately less than 10%, consistent with values reported in the literature (e.g., Yang and Shen 2010). Prior studies have shown that the normalized form drag decreases with increasing wave age c/u_* and can become negative at higher wave ages. Due to the grid resolution and the wave age considered in our simulations, the form drag is relatively weak.

To analyze the contribution of each wavenumber component of the waves to the form drag, we compute the cospectrum of pressure and wave slope and the cumulative sum of the cospectrum as in Sullivan et al. (2014). The cospectrum of form drag in the x direction is defined as

$$P_{p_m \partial h/\partial x}(k_x) = \hat{p}_m^*(k_x)\widehat{\frac{\partial h}{\partial x}}(k_x), \tag{28}$$

where $\hat{}$ denotes the Fourier coefficient, p_m is the modified pressure p/ρ_0, and the superscript * denotes the complex conjugate. The cross correlation between the pressure and the wave slope is defined as

$$R_{p_m \partial h/\partial x}(\xi') = \int_0^{L_x} \overline{p_m(\xi)\frac{\partial h}{\partial x}(\xi + \xi')}\, d\xi, \tag{29}$$

where ξ' is the distance in the horizontal direction between the pressure at the bottom ($z = h$) and the wave slope. By Eq. (29) and the definition of the Fourier transform, the cospectrum is the Fourier transform of the cross correlation. The sum of all wavenumber components of $P_{p\partial h/\partial x}$ can be written as

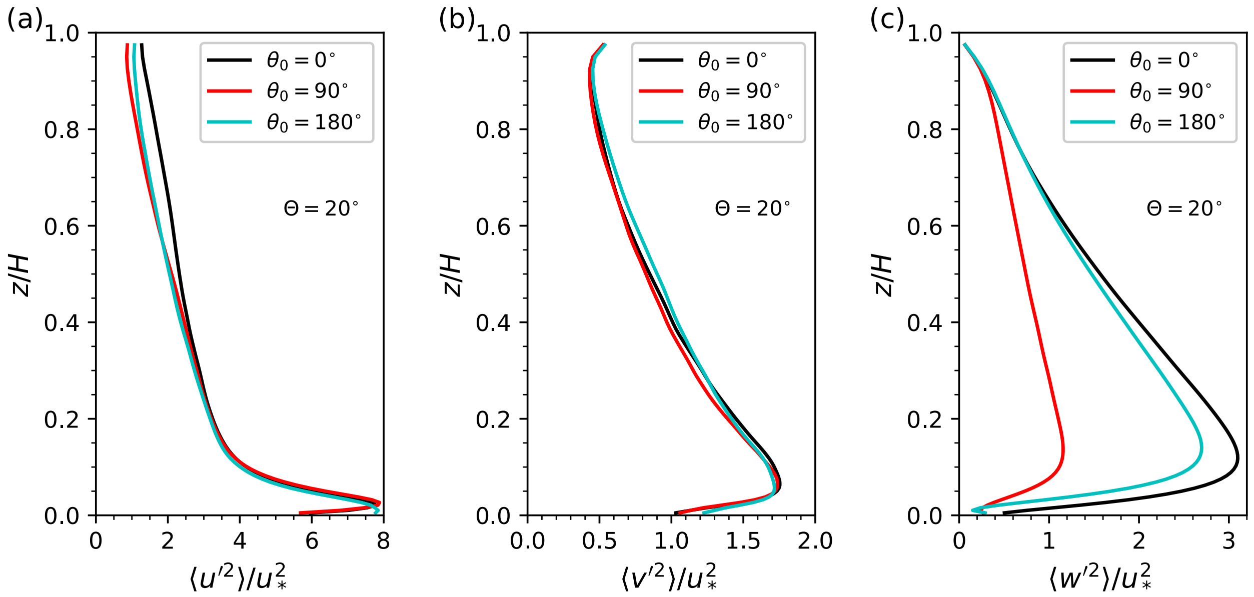

FIG. 9. Velocity variances of (a) u, (b) v, and (c) w for wave propagation directions: $\theta_0 = 0^\circ$ (black), 90° (red), and 180° (cyan), normalized by u_*^2. All three cases have the wave spreading width of $\Theta = 20^\circ$.

$$\begin{aligned}\sum_{k_x} P_{p_m \partial h/\partial x}(k_x) &= \sum_{k_x} P_{p_m \partial h/\partial x}(k_x)\exp(ik_x \cdot 0),\\ &= \mathscr{F}^{-1}(P_{p_m \partial h/\partial x})(\xi' = 0),\\ &= R_{p_m \partial h/\partial x}(\xi'),\\ &= \int_0^{L_x} \overline{p_m(\xi)\frac{\partial h}{\partial x}(\xi)d\xi},\end{aligned} \qquad (30)$$

which is the form drag. Therefore, the cumulative sum of $P_{p_m \partial h/\partial x}$ at the largest wavenumber equals the form drag, and the cumulative sum at other wavenumbers shows the contribution of different wavenumbers to the total form drag. The cospectrum can be computed in the y direction in a similar manner. The cospectra between the surface pressure and the wave slope are given in Figs. 13–15 for $\theta_0 = 0^\circ$, 90°, and 180°, respectively. The distribution of the cospectrum across wavenumbers is similar for $\theta_0 = 0^\circ$ and $\theta_0 = 180^\circ$, except in the

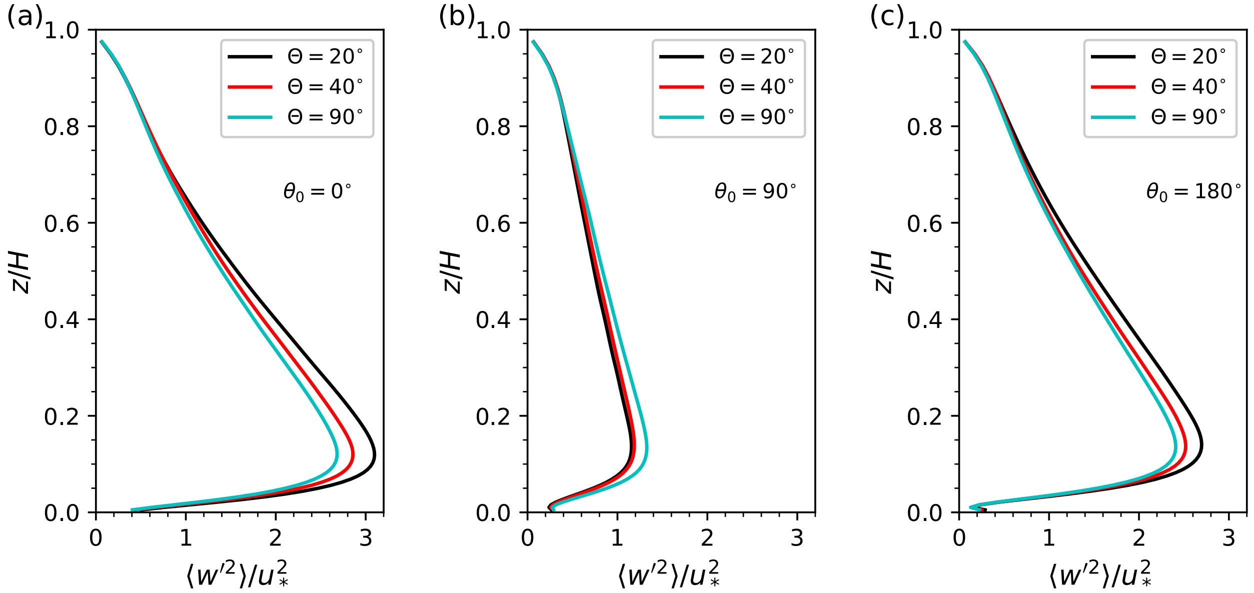

FIG. 10. Velocity variance $\langle w'^2\rangle$ for wave propagation directions: (a) $\theta_0 = 0^\circ$, (b) 90°, and (c) 180°, normalized by u_*^2. The colors black, red, and cyan represent wave spreading widths of $\Theta = 20^\circ$, 40°, and 90°, respectively.

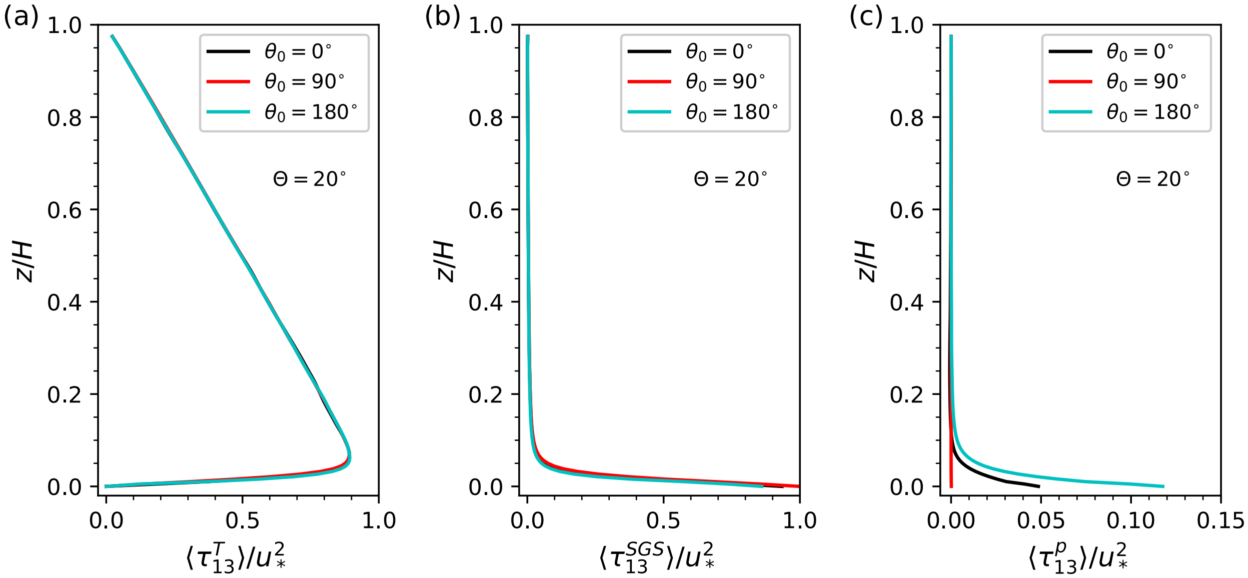

FIG. 11. Profiles of (a) Reynolds stress, (b) SGS stress, and (c) pressure stress for wave propagation directions: $\theta_0 = 0^\circ$ (black), 90° (red), and 180° (cyan), normalized by u_*^2. All cases have the wave spreading width of $\Theta = 20^\circ$.

latter, i.e., the wind-opposing case, and the magnitude of the cospectrum and its cumulative sum are almost doubled compared to the former, consistent with the form drag (Fig. 11). This difference in magnitude can also be clearly observed in Fig. 16, which compares the effect of the propagating direction on the cospectrum with Θ fixed at 20°. In both the wind-following and wind-opposing cases, the sharpest increase in the cospectrum and its cumulative sum occurs at the spectral peak wavenumber k_p, where the wave energy is most concentrated and contributes the most to the form drag. On the other hand, small-scale waves with $k > 1.5k_p$, or $\lambda < 16.7$ m, contribute significantly more to the form drag than larger-scale waves with $k < 0.5k_p$ or $\lambda > 50$ m. This is consistent with the fact that longer waves travel at a faster speed according to the dispersion relation, which is closer than shorter waves to the speed of the wind. Figure 14 shows the cospectrum between the surface pressure and the spanwise wave slope for $\theta_0 = 90^\circ$. Unlike the wind-following and wind-opposing cases, the streamwise component of the form drag in this case is negligible, whereas a nonnegligible mean flow is developed in the spanwise direction. The cospectrum and its cumulative sum are negative, indicating that the waves exert a

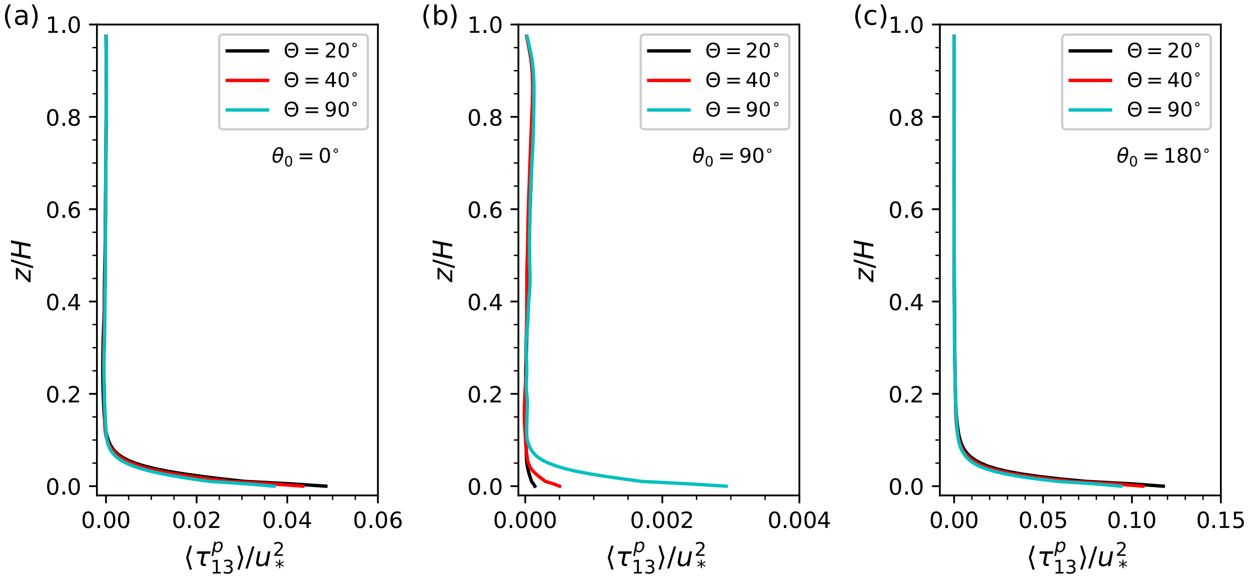

FIG. 12. Profiles of pressure stress for wave propagation directions: (a) $\theta_0 = 0^\circ$, (b) 90°, and (c) 180°, normalized by u_*^2. The colors black, red, and cyan represent wave spreading widths of $\Theta = 20^\circ$, 40°, and 90°, respectively.

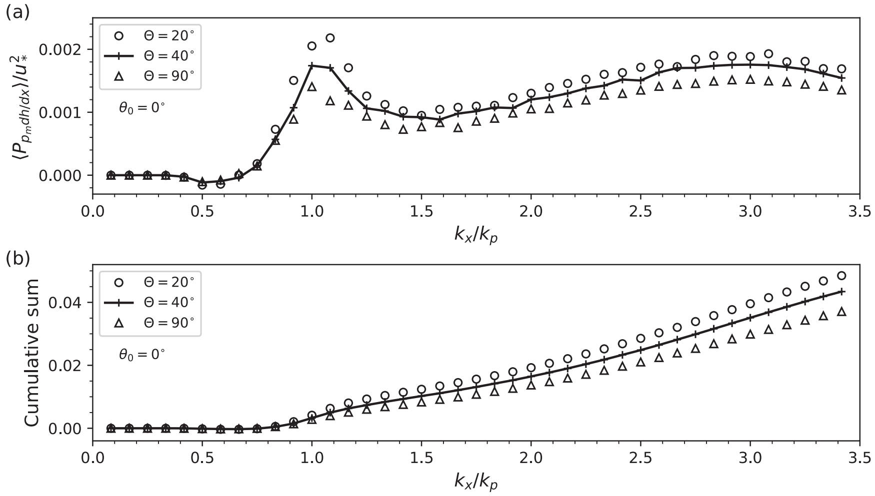

FIG. 13. (a) Cospectrum of pressure at the bottom and the wave slope and (b) the cumulative sum of the cospectrum, normalized by u_*^2 for wave propagation direction $\theta_0 = 0°$ and different spreading widths Θ.

positive force on the wind. This is because there is no forcing or mean wind in the spanwise direction, and the "drag" from waves in the spanwise direction drives the spanwise wind. Faster waves exert more drag on the wind, and thus longer waves with $k < 0.5k_p$ contribute dominantly to the drag. Similar to the effect of Θ on the vertical velocity variance (Fig. 10f) and the pressure stress (Fig. 12f), the effect of Θ on the cospectrum and its cumulative sum for the perpendicular wave is the opposite from the wind-following or wind-opposing waves. The wider the waves spread, the more they deviate from the spanwise direction, which leads to less drag in the spanwise direction. This effect is more prominent for longer waves, which contribute to most of the drag. For shorter waves, the difference in the cospectrum and its cumulative sum due to different spreading widths diminishes. The case with Θ = 20° has the largest form drag, while cases with Θ = 40° and 90° result in smaller form drag magnitudes that are nearly indistinguishable.

The interaction between the wind and the waves can also be quantified with the wave growth rate β, which is defined for flow over a monochromatic wave as (Li et al. 2000)

$$\beta = \frac{2F_p}{(ak)^2}, \tag{31}$$

where F_p is the normalized form drag:

$$F_p = \frac{1}{\lambda u_*^2}\int_0^\lambda \frac{1}{\rho} p|_{z=h}\frac{\partial h}{\partial x}dx, \tag{32}$$

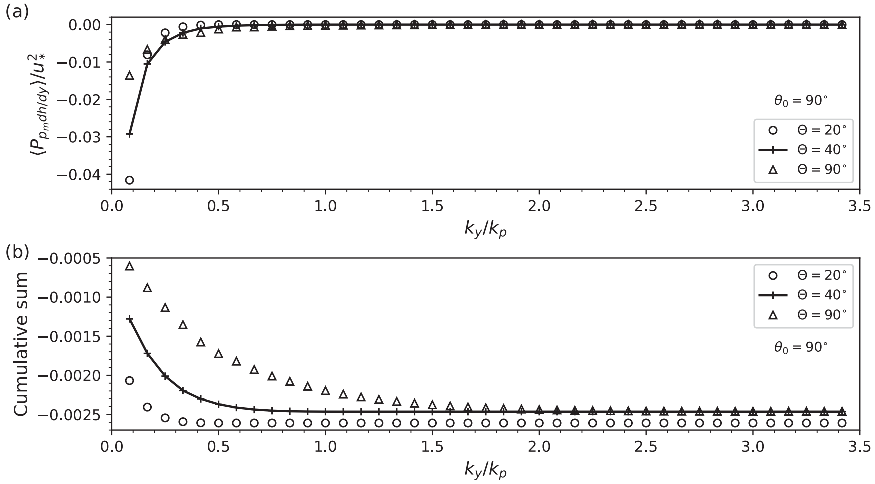

FIG. 14. (a) Cospectrum of pressure at the bottom and the wave slope and (b) the cumulative sum of the cospectrum, normalized by u_*^2 for wave propagation direction $\theta_0 = 90°$ and different spreading widths Θ.

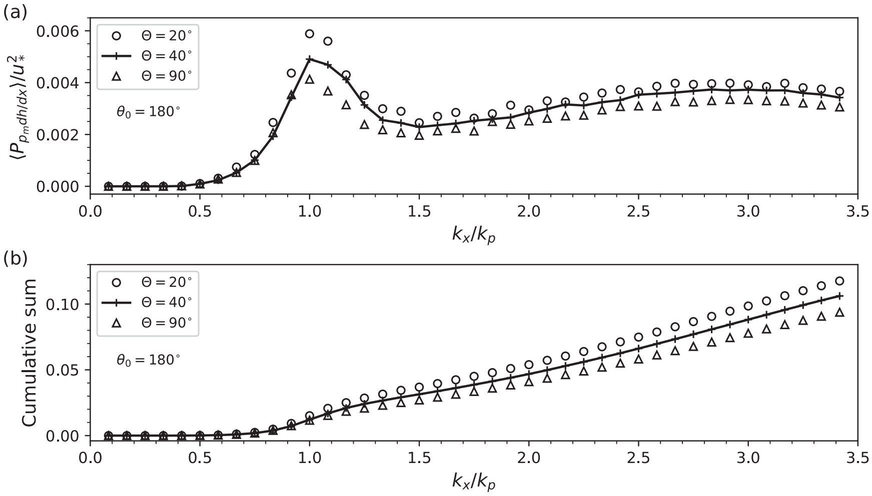

FIG. 15. (a) Cospectrum of pressure at the bottom and the wave slope and (b) the cumulative sum of the cospectrum, normalized by u_*^2 for wave propagation direction $\theta_0 = 180°$ and different spreading widths Θ.

and λ is the wavelength. To compute the wave growth rate for broadband waves, we adopt the method in Liu et al. (2009), for which

$$\beta = \frac{1}{\rho u_*}\frac{\hat{p}}{\hat{a}k_x}\sin\Delta\theta, \tag{33}$$

where $\Delta\theta$ is the phase difference between the pressure and the wave amplitude. Equation (33) can be derived by considering one wavenumber component of broadband waves $h(k) = \hat{a}\cos(kx - \omega t + \theta_h)$ and the corresponding pressure at the surface $p(k) = \hat{p}\cos(kx - \omega t + \theta_p)$, where θ_h and θ_p are the phases of the wave elevation and the pressure. Substituting $h(k)$ and $p(k)$ into Eq. (32), we obtain $F_p = 1/(2\rho u^*)\hat{p}\hat{a}k\cos\Delta\theta$. Then, by the definition of β [Eq. (31)], we arrive at Eq. (33). A similar expression for β in the spanwise direction can be obtained by performing a Fourier transform in the spanwise direction and replacing k_x in the denominator of Eq. (33) with k_y.

In Fig. 17, we show β as a function of the nondimensional wave phase speed c/u_* within the wavenumber range of $0.5k_p < k_x < 1.5k_p$. The choice of this range is based on the grid resolution analysis in the appendix to better resolve waves. In the present study, the wave age c_p/u_*, defined as the ratio between the wave phase speed of the peak frequency c_p and the air friction velocity u_*, is 11.8, as indicated by the black dashed line in Fig. 17. For each propagating direction θ_0, the growth rate is not affected by the spreading width Θ, while θ_0 has a significant influence on β. For $\theta_0 = 0°$ and 180°, β is positive and decreases smoothly with c/u_*. The magnitude and trend of β for $\theta_0 = 0°$ as a function of c/u_* are consistent

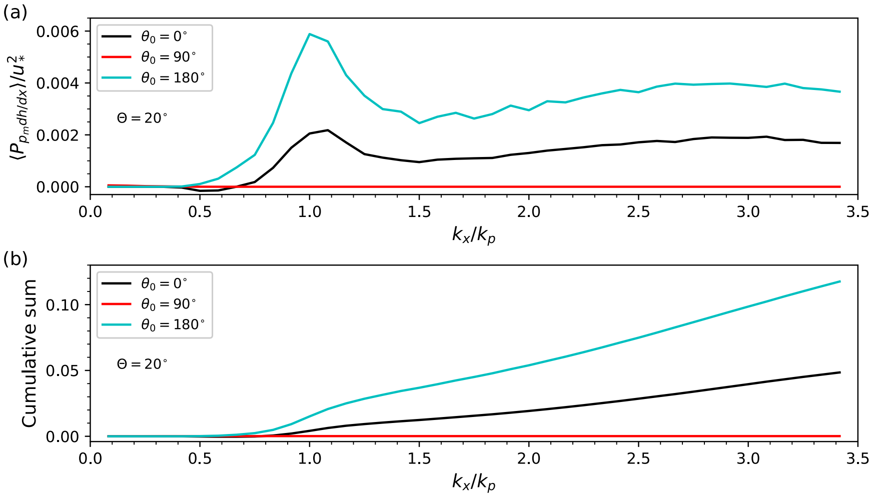

FIG. 16. (a) Cospectrum of pressure at the bottom and the wave slope and (b) the cumulative sum of the cospectrum, normalized by u_*^2 for wave spreading width of $\Theta = 20°$ and wave propagation directions: $\theta_0 = 0°$ (black), 90° (red), and 180° (blue).

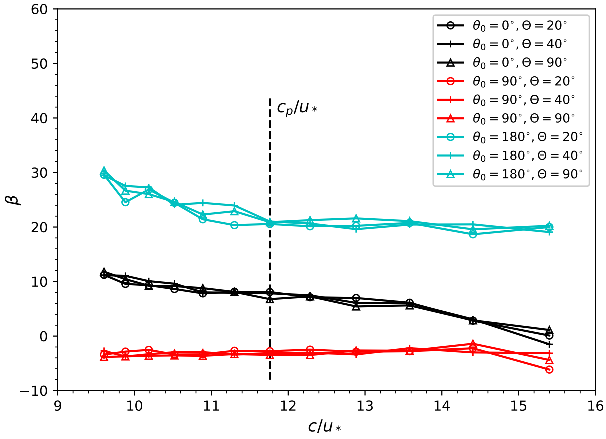

FIG. 17. Wave growth rate β vs nondimensional wave phase speed c/u_* for all nine cases.

with the literature (e.g., Kihara et al. 2007; Grare et al. 2013; Hao and Shen 2019). For $\theta_0 = 180°$, since the form drag is doubled from the case with $\theta_0 = 0°$ and the growth rate is proportional to the form drag [Eq. (31)], the growth rate is also doubled. For $\theta_0 = 90°$, c/u_* is computed for the spanwise direction. The negative form drag leads to a negative growth rate, whose magnitude also decreases with increasing c/u_*. These results are consistent with the results of the cospectra between the surface pressure and the wave slope and their cumulative sums (Figs. 13–15).

To quantify the influence of wave-propagating direction and spreading width on the total drag, we computed the bulk drag coefficient C_d based on the expression:

$$\tau_{\text{tot}} = u_*^2 = C_d U_{10}^2, \tag{34}$$

where $U_{10} = \sqrt{\langle u_{10}\rangle^2 + \langle v_{10}\rangle^2}$ is the velocity magnitude at $z = 10$ m, a height that is often used in large-scale atmospheric modeling to estimate the drag at the air–sea interface (e.g., Drennan et al. 2005; Andreas et al. 2012; Patton et al. 2019). The bulk drag coefficient can then be computed with

$$C_d = \frac{u_*^2}{U_{10}^2}. \tag{35}$$

Figure 18 shows C_d as a function of Θ for different wave propagation directions. We performed an additional run with a flat bottom surface while keeping all other parameters, including grid resolution and turbulence model, unchanged. This flat case serves as a baseline reference for evaluating the impact of explicitly resolved waves on the computed C_d value. The C_d value obtained from this additional run is denoted as the dashed line in Fig. 18. In our wall-modeled setup, the choice of $z_0 = 0.0002$ m ensures that the magnitude of C_d is $O(10^{-3})$, consistent with the measurements from the Coupled Boundary Layers Air–Sea Transfer field campaign (Edson et al. 2007), which reports C_d values at $z = 10$ m mostly falls within the range 0.001–0.003. As expected, the flat bottom surface case yields the smallest drag coefficient, as the phase-resolved ocean surface waves in other cases introduce additional surface roughness. In the present simulations, the specified wave age provides that the calculated form drag accounts for only about 10% of the total drag, with the remaining drag coming from the prescribed roughness length z_0 in the wall-modeled approach. The absolute value of C_d is highly dependent on the chosen value of z_0. The case with $\theta_0 = 180°$ has the largest drag coefficient and the case with $\theta_0 = 90°$ has the smallest, consistent with the fact that wind-opposing waves tend to slow down the wind more and waves perpendicular to the wind generate the least drag (Manzella et al. 2024). For $\Theta = 20°$, the difference between C_d at $\theta_0 = 180°$ and 90° is approximately 25%. The wave spreading width has a smaller effect on the drag coefficient. The C_d decreased by roughly 3% as Θ increases for $\theta_0 = 0°$ and roughly 5% for $\theta_0 = 180°$.

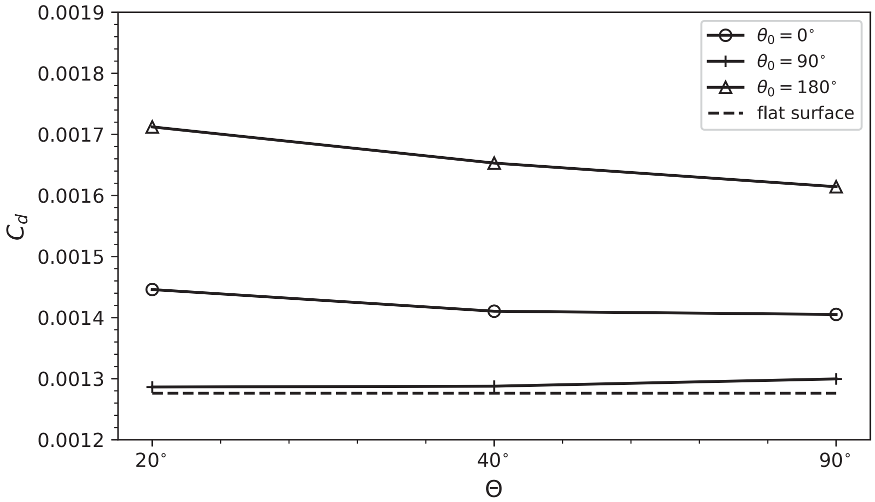

FIG. 18. Drag coefficient C_d vs wave spreading width Θ for all nine cases. The dashed line indicates the drag coefficient calculated from the flat surface case.

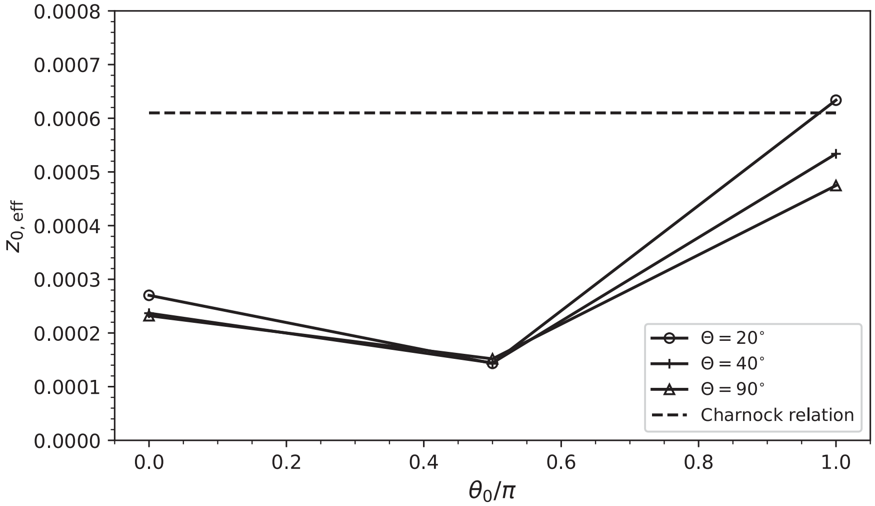

FIG. 19. The effective roughness length $z_{0,\mathrm{eff}}$ (m) vs the wave-propagating direction θ_0 for all nine cases.

The most common roughness length parameterization in atmospheric models is the Charnock relation (Charnock 1955):

$$z_{0,\mathrm{eff}} = \alpha \frac{u_*^2}{g}, \tag{36}$$

where $\alpha = 0.018$ is the Charnock parameter for offshore conditions. The Charnock parameterization is widely used for wave-parameterized models where the air–sea interface is modeled as a flat surface; in our wave-phase-resolved simulation, we explicitly incorporate the wave's deformation and movement into the model by solving the compressible LES equations in a dynamically evolving sea surface wave-fitted grid. This approach allows us to naturally capture wind–wave interactions. We compare the Charnock parameterization to our model results in Fig. 19 by computing the effective roughness length $z_{0,\mathrm{eff}}$ using the drag coefficient C_d from Eq. (35) and inverting Eq. (12), to give

$$z_{0,\mathrm{eff}} = z_{\mathrm{ref}} \exp\left(-\kappa/\sqrt{C_d}\right), \tag{37}$$

where $z_{\mathrm{ref}} = 10$ m. In the present simulations, we set the background surface roughness z_0 to 0.0002 m and set the wave age of broadband waves c_p/u_* to 11.8. For all wave spreading widths, $z_{0,\mathrm{eff}}$ is the largest at $\theta_0 = 180°$ and the smallest at $\theta_0 = 90°$, while for all propagating directions, $z_{0,\mathrm{eff}}$ decreases with increasing spreading widths, trends that are consistent with the variation in C_d shown in Fig. 18. The Charnock relation does not account for wave-propagating direction or spreading width and gives $z_{0,\mathrm{eff}} = 0.000\,61$ for all nine cases, which is very close to the value of $z_{0,\mathrm{eff}}$ from wind-opposing waves with a spreading width of 20°. The value of $z_{0,\mathrm{eff}}$ can vary by up to 25% as the spreading width changes and up to 57% as the propagating direction changes. These changes are significant and indicate the importance of wave-propagating direction and spreading width on the effective roughness length. Not only are these effects not captured by the Charnock relation, but the relation also generally overpredicts the roughness length, particularly when the waves are perpendicular to the wind, for which the Charnock relation overpredicts the roughness by more than a factor of 4. A few studies proposed new parameterization schemes for $z_{0,\mathrm{eff}}$ or the bottom drag that account for the misalignment between the wind and waves (e.g., Patton et al. 2019; Porchetta et al. 2019). However, these parameterizations are based on datasets in parameter regimes that preclude comparison to our results or the Charnock relation.

4. Conclusions

In this work, we extended the implementation of the coupled wave and WRF–LES model to simulate the ABL over broadband waves. We use the JONSWAP spectrum to generate wave fields with different propagating directions and wave spreading widths to investigate their influence on the overlying wind. Nine cases are analyzed with propagating directions $\theta_0 = 0°$, 90°, and 180°, each with wave spreading widths $\Theta = 20°$, 40° and 90°. To the best of our knowledge, this is the first study in which broadband wave fields with different propagating directions and spreading widths are employed in LES of the ABL. Additionally, the waves are physically oriented with an angle to the streamwise direction, which is different from previous studies that apply pressure gradient forcing in both the streamwise and spanwise directions to achieve wind–wave misalignment (Husain et al. 2022b; Deskos et al. 2022).

Our results show that for all cases, the wind and waves are strongly correlated, and the influence of waves on the wind extends to a height of roughly one peak wavelength. The propagating direction of the waves has significant effects on the mean wind, wind turbulence, and pressure stress, while the effect of the spreading width is smaller. Wind-opposing waves doubled the form drag compared to the wind-following waves. For wind-following and wind-opposing waves, the wider the waves spread, the smaller the form drag in the streamwise direction and the reverse applies to waves perpendicular to the wind. The analysis of the cospectrum between the surface pressure and the wave slope reveals that shorter waves contribute more to the form drag than longer waves. Finally, we found that the bulk drag coefficient can vary by up to 25% with different wave-propagating directions, whereas the effect of the spreading width on the bulk drag coefficient is less than 5%. These effects are more pronounced for the effective roughness length based on the present research, where the background roughness is set to 0.0002 m. The effective roughness length is modified relatively by up to 57% due to wave propagation direction and 25% due to the wave spreading width. Comparison to the commonly used Charnock relation shows that it generally overestimates the roughness length, indicating that many coupled ocean–atmosphere models could be overestimating the ocean–atmosphere drag. While our study demonstrates the importance of wave direction and spread, more studies are needed over broader parameter spaces to develop general parameterizations for ocean–atmosphere drag, including varying wave ages and applications to realistic meteorological conditions including Coriolis, heat, and moisture effects.

Acknowledgments. This work was performed under the auspices of the U.S. Department of Energy by Lawrence Livermore National Laboratory under Contract DE-AC52-07NA27344 with document number LLNL-JRNL-866068 and supported by the Wind Energy Technologies Office. Support was also provided by the Office of Naval Research Grant N00014-20-1-2707 and N00014-24-1-2707.

Data availability statement. All data and code used in this study will be available upon request.

APPENDIX

Sensitivity Analysis

a. Grid resolution in WRF simulation

We conduct a numerical experiment to investigate the effect of grid resolution on the simulation of wind over broadband waves. The physical parameters for this experiment are the same as the previous simulation in which the dominant propagating direction of the broadband wave field θ_0 is 0° relative to the positive streamwise direction, and the spreading width Θ is 20°. In the previous simulation, we use a grid with 128 × 128 × 80 points in the streamwise, spanwise, and vertical directions. In the higher resolution case, we use a 256 × 256 × 160 grid. This resolution represents a doubling of grid points in each direction compared to the other simulations conducted in this study. The time step is reduced to 0.0042 s due to the CFL constraint in terms of the sound speed. Simulation results show that the mean streamwise velocity profiles agree between different resolutions, as shown in the blue and purple lines of Fig. A1.

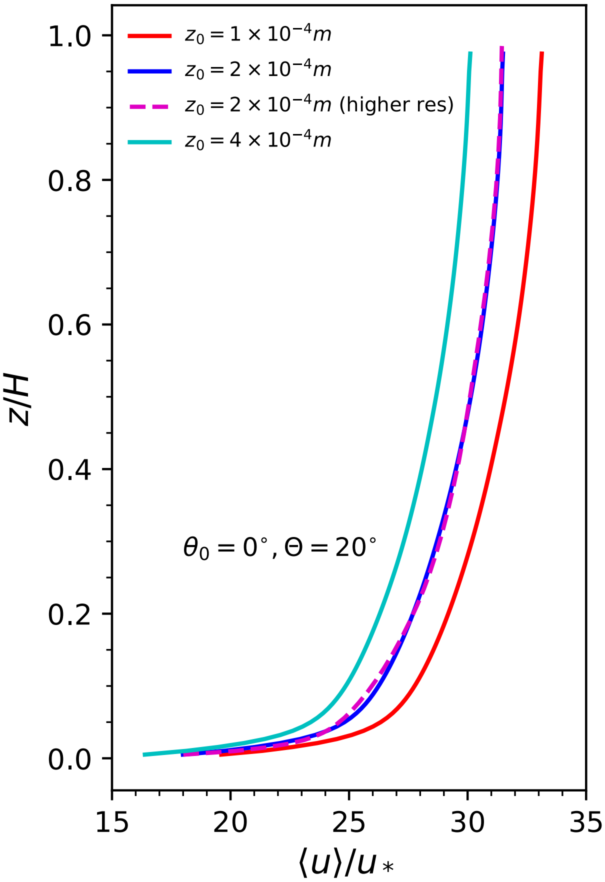

FIG. A1. Mean streamwise velocity normalized by u_* for surface roughness z_0 = 0.0001 m (red), z_0 = 0.0002 m (blue), and z_0 = 0.0004 m (cyan). Solid lines are cases with a grid of 128 × 128 × 60 points. The dashed purple line represents the higher resolution case with z_0 = 0.0002 m and a grid of 256 × 256 × 160 points. Both cases have $\theta_0 = 0^\circ$ and $\Theta = 20^\circ$.

We further compare the wave growth rate β as a function of streamwise wavenumber k_x between the two simulations. As shown in Fig. A2, the wave growth rate β within the range of $0.5k_p < k_x < 1.5k_p$ is the same for both resolutions. This is because in the coaser simulation case, the peak wave component is resolved with 11 points per wavelength, and the wave with a wavenumber of $1.5k_p$ is resolved with roughly seven

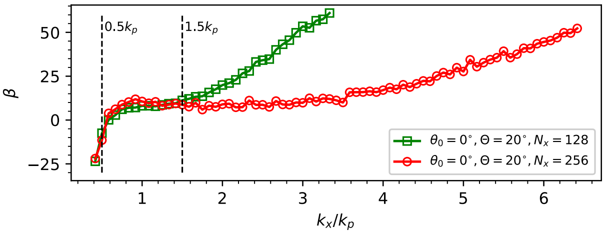

FIG. A2. The wave growth rate β vs the streamwise wavenumber k_x normalized by the peak wavenumber k_p. The green line and the red line represent cases with grids of 128 × 128 × 80 and 256 × 256 × 160 points, respectively. All cases have $\theta_0 = 0^\circ$ and $\Theta = 20^\circ$.

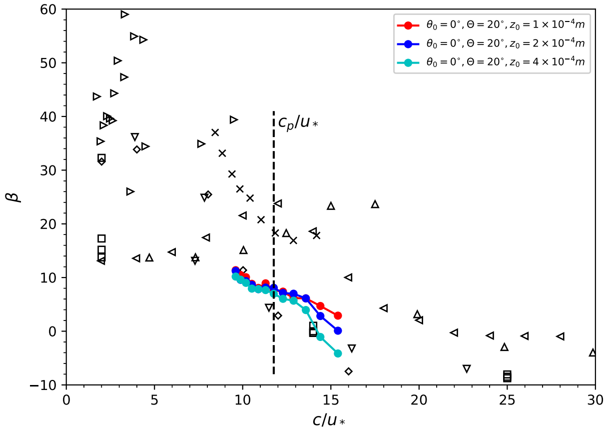

FIG. A3. The wave growth rate β vs the nondimensional wave phase speed c/u_* for different background surface roughness lengths z_0. The red, blue, and cyan lines show the cases with surface roughness lengths z_0 of 0.0001, 0.0002, and 0.0004 m, respectively. The dashed line indicates the wave age c_p/u_*. All cases have $\theta_0 = 0°$, $\Theta = 20°$, and the wave age $c_p/u_* = 11.8$. Other results in literature are plotted for comparison: ▷, experiments by Grare et al. (2013); Δ, Reynolds averaged Navier–Stokes (RANS) simulations by Mastenbroek (1996); ◁, RANS (Li et al. 2000); ∇, DNS (Sullivan et al. 2000); ◊, DNS (Kihara et al. 2007); □, DNS (Yang and Shen 2010); and ×, LES (Hao and Shen 2019).

points. Shorter waves have fewer than four points per wavelength and thus are not well resolved. On the other hand, there are 12 peak wavelengths in the streamwise direction of the domain, while only six wavelengths with $k_p/2$. The statistics are thus more reliable for waves having more ensembles in the streamwise direction.

b. Sensitivity analysis of background surface roughness length

In the present study, the background surface roughness length z_0 accounts for the effects of smaller unresolved waves and viscous stress [see discussions in Sullivan et al. (2014), Manzella et al. (2024)], which is necessary for the wall-modeled approach in LES. The roughness effects of resolved waves are directly obtained through the interactions between the wind and the resolved waves. The z_0 value of 0.0002 m is a typical value that has been wildly used in wave-phase-resolved simulations (e.g., Sullivan et al. 2014; Jiang et al. 2016; Hao and Shen 2019). Here, we investigate the effects of background surface roughness length z_0 on the airflow statistics and wave growth rate by varying the roughness length. We conduct additional simulations using z_0 values of 0.0001 and 0.0004 m using a 128 × 128 × 80 grid. The other physical parameters of wind and waves remain the same as in the case with a wave primary propagation direction relative to the wind $\theta_0 = 0°$ and a wave directional spreading width $\Theta = 20°$. We adopt the surface roughness length $z_0 = 0.0002$ m in the original simulations. Figure A1 compares the mean streamwise wind velocity among the cases with different z_0 values and shows that the increase in surface roughness length can reduce the mean streamwise velocity of the wind, which is consistent with Husain et al. (2019). We further compare the wave growth rate β for these cases. As shown in Fig. A3, the wave growth rate β decreases with increasing nondimensional wave phase speed c/u_*, which is consistent with other numerical simulations in literature (e.g., Mastenbroek 1996; Li et al. 2000; Sullivan et al. 2000; Kihara et al. 2007; Yang and Shen 2010; Hao and Shen 2019). Experiments by Grare et al. (2013) also report higher wave growth rates at smaller wave ages. The wave growth rates at the wave age $c_p/u_* = 11.8$ are close to eight for all three cases, with a standard deviation of only 6% of the mean. This indicates that the background surface roughness length plays a minor role in determining the wave growth rate at the peak wave frequency in this study.

REFERENCES

Aiyer, A. K., L. Deike, and M. E. Mueller, 2023: A sea surface–based drag model for large-eddy simulation of wind–wave interaction. *J. Atmos. Sci.*, **80**, 49–62, https://doi.org/10.1175/JAS-D-21-0329.1.

Andreas, E. L., L. Mahrt, and D. Vickers, 2012: A new drag relation for aerodynamically rough flow over the ocean. *J. Atmos. Sci.*, **69**, 2520–2537, https://doi.org/10.1175/JAS-D-11-0312.1.

Ardhuin, F., T. H. C. Herbers, K. P. Watts, G. P. van Vledder, R. Jensen, and H. C. Graber, 2007: Swell and slanting-fetch effects on wind wave growth. *J. Phys. Oceanogr.*, **37**, 908–931, https://doi.org/10.1175/JPO3039.1.

Ayala, M., Z. Sadek, O. Ferčák, R. B. Cal, D. F. Gayme, and C. Meneveau, 2024: A moving surface drag model for les of wind over waves. *Bound.-Layer Meteor.*, **190**, 39, https://doi.org/10.1007/s10546-024-00884-8.

Belcher, S. E., and J. C. R. Hunt, 1998: Turbulent flow over hills and waves. *Annu. Rev. Fluid Mech.*, **30**, 507–538, https://doi.org/10.1146/annurev.fluid.30.1.507.

——, T. M. J. Newley, and J. C. R. Hunt, 1993: The drag on an undulating surface induced by the flow of a turbulent boundary layer. *J. Fluid Mech.*, **249**, 557–596, https://doi.org/10.1017/S0022112093001296.

Bowers, J. A., I. D. Morton, and G. I. Mould, 2000: Directional statistics of the wind and waves. *Appl. Ocean Res.*, **22**, 13–30, https://doi.org/10.1016/S0141-1187(99)00025-5.

Buckley, M. P., and F. Veron, 2016: Structure of the airflow above surface waves. *J. Phys. Oceanogr.*, **46**, 1377–1397, https://doi.org/10.1175/JPO-D-15-0135.1.

Burgers, G., and V. K. Makin, 1993: Boundary-layer model results for wind-sea growth. *J. Phys. Oceanogr.*, **23**, 372–385, https://doi.org/10.1175/1520-0485(1993)023<0372:BLMRFW>2.0.CO;2.

Cao, T., B.-Q. Deng, and L. Shen, 2020: A simulation-based mechanistic study of turbulent wind blowing over opposing water waves. *J. Fluid Mech.*, **901**, A27, https://doi.org/10.1017/jfm.2020.591.

——, X. Liu, X. Xu, and B. Deng, 2023: Investigation on mechanisms of fast opposing water waves influencing overlying wind using simulation and theoretical models. *Phys. Fluids*, **35**, 015148, https://doi.org/10.1063/5.0132131.

——, and L. Shen, 2021: A numerical and theoretical study of wind over fast-propagating water waves. *J. Fluid Mech.*, **919**, A38, https://doi.org/10.1017/jfm.2021.416.

Charnock, H., 1955: Wind stress on a water surface. *Quart. J. Roy. Meteor. Soc.*, **81**, 639–640, https://doi.org/10.1002/qj.49708135027.

Deskos, G., S. Ananthan, and M. A. Sprague, 2022: Direct numerical simulations of turbulent flow over misaligned traveling waves. *Int. J. Heat Fluid Flow*, **97**, 109029, https://doi.org/10.1016/j.ijheatfluidflow.2022.109029.

Donelan, M. A., J. Hamilton, and W. H. Hui, 1985: Directional spectra of wind-generated ocean waves. *Philos. Trans. Roy. Soc.*, **A315**, 509–562, https://doi.org/10.1098/rsta.1985.0054.

Drennan, W. M., P. K. Taylor, and M. J. Yelland, 2005: Parameterizing the sea surface roughness. *J. Phys. Oceanogr.*, **35**, 835–848, https://doi.org/10.1175/JPO2704.1.

Druzhinin, O. A., Y. I. Troitskaya, and S. S. Zilitinkevich, 2012: Direct numerical simulation of a turbulent wind over a wavy water surface. *J. Geophys. Res.*, **117**, C00J05, https://doi.org/10.1029/2011JC007789.

Edson, J., and Coauthors, 2007: The coupled boundary layers and air–sea transfer experiment in low winds. *Bull. Amer. Meteor. Soc.*, **88**, 341–356, https://doi.org/10.1175/BAMS-88-3-341.

Fischer, T., P. Rainey, E. Bossanyi, and M. Kühn, 2011: Study on control concepts suitable for mitigation of loads from misaligned wind and waves on offshore wind turbines supported on monopiles. *Wind Eng.*, **35**, 561–573, https://doi.org/10.1260/0309-524X.35.5.561.

Grare, L., W. L. Peirson, H. Branger, J. W. Walker, J.-P. Giovanangeli, and V. Makin, 2013: Growth and dissipation of wind-forced, deep-water waves. *J. Fluid Mech.*, **722**, 5–50, https://doi.org/10.1017/jfm.2013.88.

Hanley, K. E., S. E. Belcher, and P. P. Sullivan, 2010: A global climatology of wind–wave interaction. *J. Phys. Oceanogr.*, **40**, 1263–1282, https://doi.org/10.1175/2010JPO4377.1.

Hao, X., and L. Shen, 2019: Wind–wave coupling study using LES of wind and phase-resolved simulation of nonlinear waves. *J. Fluid Mech.*, **874**, 391–425, https://doi.org/10.1017/jfm.2019.444.

Hara, T., and P. P. Sullivan, 2015: Wave boundary layer turbulence over surface waves in a strongly forced condition. *J. Phys. Oceanogr.*, **45**, 868–883, https://doi.org/10.1175/JPO-D-14-0116.1.

Hasselmann, K., and Coauthors, 1973: *Measurements of Wind-Wave Growth and Swell Decay during the Joint North Sea Wave Project (JONSWAP).* Deutsches Hydrographisches Institut, 95 pp.

Hildebrandt, A., B. Schmidt, and S. Marx, 2019: Wind-wave misalignment and a combination method for direction-dependent extreme incidents. *Ocean Eng.*, **180**, 10–22, https://doi.org/10.1016/j.oceaneng.2019.03.034.

Husain, N. T., T. Hara, M. P. Buckley, K. Yousefi, F. Veron, and P. P. Sullivan, 2019: Boundary layer turbulence over surface waves in a strongly forced condition: LES and observation. *J. Phys. Oceanogr.*, **49**, 1997–2015, https://doi.org/10.1175/JPO-D-19-0070.1.

——, ——, and P. P. Sullivan, 2022a: Wind turbulence over misaligned surface waves and air–sea momentum flux. Part I: Waves following and opposing wind. *J. Phys. Oceanogr.*, **52**, 119–139, https://doi.org/10.1175/JPO-D-21-0043.1

——, ——, and ——, 2022b: Wind turbulence over misaligned surface waves and air–sea momentum flux. Part II: Waves in oblique wind. *J. Phys. Oceanogr.*, **52**, 141–159, https://doi.org/10.1175/JPO-D-21-0044.1.

Jiang, Q., P. Sullivan, S. Wang, J. Doyle, and L. Vincent, 2016: Impact of swell on air–sea momentum flux and marine boundary layer under low-wind conditions. *J. Atmos. Sci.*, **73**, 2683–2697, https://doi.org/10.1175/JAS-D-15-0200.1.

Johnson, H. K., J. Hojstrup, H. J. Vested, and S. E. Larsen, 1998: On the dependence of sea surface roughness on wind waves. *J. Phys. Oceanogr.*, **28**, 1702–1716, https://doi.org/10.1175/1520-0485(1998)028<1702:OTDOSS>2.0.CO;2.

Kalvig, S., E. Manger, B. H. Hjertager, and J. B. Jakobsen, 2014: Wave influenced wind and the effect on offshore wind turbine performance. *Energy Procedia*, **53**, 202–213, https://doi.org/10.1016/j.egypro.2014.07.229.

Kihara, N., H. Hanazaki, T. Mizuya, and H. Ueda, 2007: Relationship between airflow at the critical height and momentum transfer to the traveling waves. *Phys. Fluids*, **19**, 015102, https://doi.org/10.1063/1.2409736.

Koukoura, C., C. Brown, A. Natarajan, and A. Vesth, 2016: Cross-wind fatigue analysis of a full scale offshore wind turbine in the case of wind–wave misalignment. *Eng. Struct.*, **120**, 147–157, https://doi.org/10.1016/j.engstruct.2016.04.027.

Li, P. Y., D. Xu, and P. A. Taylor, 2000: Numerical modelling of turbulent airflow over water waves. *Bound.-Layer Meteor.*, **95**, 397–425, https://doi.org/10.1023/A:1002677312259.

Li, T., and L. Shen, 2022: The principal stage in wind-wave generation. *J. Fluid Mech.*, **934**, A41, https://doi.org/10.1017/jfm.2021.1153.

——, and ——, 2023: Direct numerical evidence of the Phillips initial stage and its antecedent during wind-wave generation. *Commun. Phys.*, **6**, 314, https://doi.org/10.1038/s42005-023-01430-7.

Li, X., C. Zhu, Z. Fan, X. Chen, and J. Tan, 2020: Effects of the yaw error and the wind-wave misalignment on the dynamic characteristics of the floating offshore wind turbine. *Ocean Eng.*, **199**, 106960, https://doi.org/10.1016/j.oceaneng.2020.106960.

Liu, S., A. Kermani, L. Shen, and D. K. P. Yue, 2009: Investigation of coupled air-water turbulent boundary layers using direct numerical simulations. *Phys. Fluids*, **21**, 062108, https://doi.org/10.1063/1.3156013.

Longuet-Higgins, M. S., 1963: The effect of non-linearities on statistical distributions in the theory of sea waves. *J. Fluid Mech.*, **17**, 459–480, https://doi.org/10.1017/S0022112063001452.

Manzella, E., T. Hara, and P. P. Sullivan, 2024: Reduction of drag coefficient due to misaligned wind-waves. *J. Geophys. Res. Oceans*, **129**, e2023JC020593, https://doi.org/10.1029/2023JC020593.

Mastenbroek, C., 1996: Wind-wave interaction. Ph.D. thesis, Delft Technical University, 118 pp.

Moon, I.-J., T. Hara, I. Ginis, S. E. Belcher, and H. L. Tolman, 2004: Effect of surface waves on air–sea momentum exchange. Part I: Effect of mature and growing seas. *J. Atmos. Sci.*, **61**, 2321–2333, https://doi.org/10.1175/1520-0469(2004)061<2321:EOSWOA>2.0.CO;2.

Patton, E. G., P. P. Sullivan, B. Kosović, J. Dudhia, L. Mahrt, M. Zagar, and T. Marić, 2019: On the influence of swell propagation angle on surface drag. *J. Appl. Meteor. Climatol.*, **58**, 1039–1059, https://doi.org/10.1175/JAMC-D-18-0211.1.

Porchetta, S., O. Temel, D. Muñoz-Esparza, J. Reuder, J. Monbaliu, J. Van Beeck, and N. van Lipzig, 2019: A new roughness length parameterization accounting for wind–wave (MIS) alignment. *Atmos. Chem. Phys.*, **19**, 6681–6700, https://doi.org/10.5194/acp-19-6681-2019.

Shen, L., X. Zhang, D. K. Yue, and M. S. Triantafyllou, 2003: Turbulent flow over a flexible wall undergoing a streamwise travelling wave motion. *J. Fluid Mech.*, **484**, 197–221, https://doi.org/10.1017/S0022112003004294.

Skamarock, W. C., and Coauthors, 2019: A description of the advanced research WRF model version 4. NCAR Tech. Note NCAR/TN-556+STR, 145 pp., https://doi.org/10.5065/1dfh-6p97.

Sullivan, P. P., and J. C. McWilliams, 2010: Dynamics of winds and currents coupled to surface waves. *Annu. Rev. Fluid Mech.*, **42**, 19–42, https://doi.org/10.1146/annurev-fluid-121108-145541.

——, ——, and C.-H. Moeng, 2000: Simulation of turbulent flow over idealized water waves. *J. Fluid Mech.*, **404**, 47–85, https://doi.org/10.1017/S0022112099006965.

——, J. B. Edson, T. Hristov, and J. C. McWilliams, 2008: Large-eddy simulations and observations of atmospheric marine boundary layers above nonequilibrium surface waves. *J. Atmos. Sci.*, **65**, 1225–1245, https://doi.org/10.1175/2007JAS2427.1.

——, J. C. McWilliams, and E. G. Patton, 2014: Large-eddy simulation of marine atmospheric boundary layers above a spectrum of moving waves. *J. Atmos. Sci.*, **71**, 4001–4027, https://doi.org/10.1175/JAS-D-14-0095.1.

Taylor, P. K., and M. J. Yelland, 2001: The dependence of sea surface roughness on the height and steepness of the waves. *J. Phys. Oceanogr.*, **31**, 572–590, https://doi.org/10.1175/1520-0485(2001)031<0572:TDOSSR>2.0.CO;2.

Wei, K., S. R. Arwade, A. T. Myers, V. Valamanesh, and W. Pang, 2017: Effect of wind and wave directionality on the structural performance of non-operational offshore wind turbines supported by jackets during hurricanes. *Wind Energy*, **20**, 289–303, https://doi.org/10.1002/we.2006.

Wright, C. W., and Coauthors, 2001: Hurricane directional wave spectrum spatial variation in the open ocean. *J. Phys. Oceanogr.*, **31**, 2472–2488, https://doi.org/10.1175/1520-0485(2001)031<2472:HDWSSV>2.0.CO;2.

Yang, D., and L. Shen, 2009: Characteristics of coherent vortical structures in turbulent flows over progressive surface waves. *Phys. Fluids*, **21**, 125106, https://doi.org/10.1063/1.3275851.

——, and ——, 2010: Direct-simulation-based study of turbulent flow over various waving boundaries. *J. Fluid Mech.*, **650**, 131–180, https://doi.org/10.1017/S0022112009993557.

——, C. Meneveau, and L. Shen, 2013: Dynamic modelling of sea-surface roughness for large-eddy simulation of wind over ocean wavefield. *J. Fluid Mech.*, **726**, 62–99, https://doi.org/10.1017/jfm.2013.215.

——, ——, and ——, 2014: Large-eddy simulation of offshore wind farm. *Phys. Fluids*, **26**, 025101, https://doi.org/10.1063/1.4863096.

Zhu, P., T. Li, J. D. Mirocha, R. S. Arthur, Z. Wu, and O. B. Fringer, 2023: A moving-wave implementation in WRF to study the impact of surface water waves on the atmospheric boundary layer. *Mon. Wea. Rev.*, **151**, 2883–2903, https://doi.org/10.1175/MWR-D-23-0077.1.